

AD-A245 320

2



SUMMARY REPORT

Early Stages of Interface Formation at Compound Semiconductor Surfaces
Studied by Scanning Tunneling Microscopy

January 1991 - October 1991

Grant # N00014-89-J-3029

DTIC
ELECTE
FEB 03 1992
S D D

Michael B. Weimer

Department of Physics
Texas A&M University
College Station, TX 77843-4242

This document has been approved
for public release and its
distribution is unlimited.

92-01921



31 1 19 007

The materials contained in this report were presented to Dr. Richard G. Brandt, the sponsoring Scientific Officer, as part of an October 9, 1991 site visit to our laboratory in the Physics Department at Texas A&M University. The information is largely pictorial in form, and is divided into four sections. Comments pertinent to the individual figures may be found in each of Sections II-IV.

Section I begins with a reprint entitled *The Image Potential in Scanning Tunneling Microscopy of Semiconductor Surfaces* which was published in the Journal of Vacuum Science and Technology as part of the proceedings for PCSI-18. A comprehensive and more extensive account of this work is presented in an accompanying article entitled *Internal Image Potential in Semiconductors: Effect on Scanning Tunneling Microscopy* which was recently submitted to Physical Review. These papers are the product of our collaboration with the theoretical group of Dr. Roland Allen.

Section II traces the development of our efforts to design and assemble a versatile ultra high vacuum apparatus for multi-technique surface analysis, tunneling microscopy, and *in-situ* sample preparation. Aspects of the design process facilitated by access to advanced computer-based software packages are highlighted. Particular examples include three-dimensional visualization of the complete *in-vacuo* sample transfer and manipulation scheme, as well as finite-element modeling of structural modes relevant to the optimization of system rigidity for vibration isolation.

Test data demonstrating operation of the Perkin-Elmer 15-155 Cylindrical Mirror Analyzer installed in our UHV system for Auger Electron Spectroscopy are presented in Section III.

Section IV documents some preliminary imaging and spectroscopic data obtained using a Scanning Tunneling Microscope (STM) delivered to us in late April by Omicron Vakuumphysik. This instrument has been specially modified to facilitate implementation of Ballistic Electron Emission Microscopy (BEEM). Photographs detailing the flange-mounted STM stage, both alone and in relation to the remainder of the UHV system, may be found in Section I.

The individuals responsible for carrying out our ONR sponsored program during this past year, and whose efforts have led to the results reported here, are listed on the following page.

PERSONNEL

PRINCIPAL INVESTIGATOR

Dr. Michael B. Weimer (Physics)

POSTDOCTORAL RESEARCH FELLOWS

Dr. Richard Wilkins (Physics)

GRADUATE STUDENTS

Mr. George Lengel (Physics)
Mr. Geoffrey Brown (Physics)
Mr. Sandip Barua (Computer Science)

UNDERGRADUATE STUDENTS

Mr. William M. Megarity (Aeronautical Engineering)



Accession For	
NTIS GRA&I	<input checked="" type="checkbox"/>
DFC TAB	<input type="checkbox"/>
Unannounced	<input type="checkbox"/>
Justification	
By _____	
Date (Mo/Do/YY)	
Availability Codes	
Dist	Availability Codes
A-1	

Statement A per telecon
Richard Brandt ONR/Code 1112
Arlington, VA

NWW 1/31/92

Section I

REPRINTS

The image potential in scanning tunneling microscopy of semiconductor surfaces

Z.-H. Huang, M. Weimer, and R. E. Allen

Department of Physics, Texas A&M University, College Station, Texas 77843

(Received January 29, 1991; accepted April 17, 1991)

A semiclassical screening theory for semiconductors is used to treat the image potential throughout a one-dimensional metal-vacuum-semiconductor junction in the absence of surface states. The image interaction due to induced surface charge at the semiconductor-vacuum interface produces an effective band bending in the semiconductor interior, whose influence on electron tunneling through the junction is investigated. In particular, we examine the effect of this extra potential on STM measurements of the apparent tunneling barrier at unpinned semiconductor surfaces, and consider *n*-type, H-terminated Si(111) as a specific example. In the instance where tip-induced band bending may be neglected, we find the role of the image potential in metal-vacuum semiconductor tunneling to be qualitatively similar to its role in metal-vacuum-metal tunneling: The experimentally determined barrier height—obtained from the logarithmic derivative of the tunneling current with respect to tip-sample separation—deviates little from the electron affinity of the semiconductor, while the theoretical barrier height exhibits a stronger dependence on the vacuum gap width. The origin of this behavior appears to lie in the fact that while the image interaction in the semiconductor may be long range, the image induced tunneling barrier is not.

An extra electron placed in a polarizable medium always induces a redistribution of charge. Near a surface or interface, the collective response of other electrons to this external perturbation is a net accumulation of charge at the interface. The image potential describes the interaction of the extra electron with that induced surface charge.

It has been a matter of some interest whether or not the scanning tunneling microscope (STM), with its precisely controllable vacuum gap, might provide a unique experimental opportunity to study the role of image interactions in electron tunneling. The question has been thoroughly addressed both theoretically and experimentally for the case of metal-vacuum-metal (MVM) tunneling.¹⁻⁷ In the simplest approximation, one models the STM as two planar, parallel, electrodes, separated by a distance *s*, and calculates the classical correction to the tunneling potential using the multiple-image method.^{1,2} The resulting barrier height is only slightly affected at large separations, but is significantly reduced when *s* is the order of a few angstroms. Similar conclusions may be drawn from more sophisticated density-functional calculations.^{3,4} The quantity determined in STM measurements, however, is an apparent barrier height, Φ_A , defined by³

$$\Phi_A = [(-1/A)d \ln I/ds]^2. \quad (1)$$

Here *I* is the tunnel current, *s* is the vacuum gap width, and $A = 1.025 \text{ eV}^{-1/2} \text{ \AA}^{-1}$. Experimental results^{4,5} indicate the logarithm of *I* vs *s* is nearly linear over a wide range, so that Φ_A is essentially independent of gap width, and has a value close to the average work function of tip and sample electrodes. As Binnig *et al.*⁴ and Coombs *et al.*⁶ explain, it appears that Φ_A is insensitive to the image interaction because of a cancellation, between the distance dependent barrier height and the rate of change of this barrier height with increasing gap separation, that is specific to the form of the image potential.

If one replaces the metal sample electrode with a nondegenerate semiconductor, the classical image force in the vacuum is slightly reduced due to the semiconductor's finite polarizability, but this does not qualitatively alter the form of the potential in this region. A more important distinction, however, is that a long range potential also extends into the semiconductor interior, and this results in an effective band bending which becomes significant for electrons near the semiconductor-vacuum interface.^{8,9} This band bending contributes to the overall tunneling barrier experienced by electrons originating from the bottom of the conduction band in *n*-type material. It has previously been noted¹⁰ that the space charge induced by the presence of a metal tip near an unpinned semiconductor surface is highly sensitive to the distance between tip and sample, and that varying this distance has a profound effect on both the tunneling probability and the experimentally inferred barrier height. We may inquire, then, whether the effective band bending associated with image interactions in a metal-vacuum-semiconductor (MVS) junction is similarly sensitive to the gap spacing, and therefore presents a distinctive signature of the image interaction which is unavailable in MVM tunneling. It is the purpose of this paper to address that question.

In what follows, we derive a semiclassical expression for the image potential experienced by a single electron traversing an ideal, nondegenerate MVS junction without surface states. This potential is used to calculate a tunneling transmission probability by solving a one electron Schrödinger equation in the effective mass approximation. An apparent barrier height Φ_A is then extracted with the aid of Eq. (1) for the specific case of an *n*-type hydrogen-terminated Si(111)-Au system when the applied bias has been chosen to eliminate tip-induced band bending.

Expressions for the classical image potential in an ideal metal-insulator-semiconductor (MIS) junction similar to that shown in Fig. 1 have been previously derived.^{8,9} It is

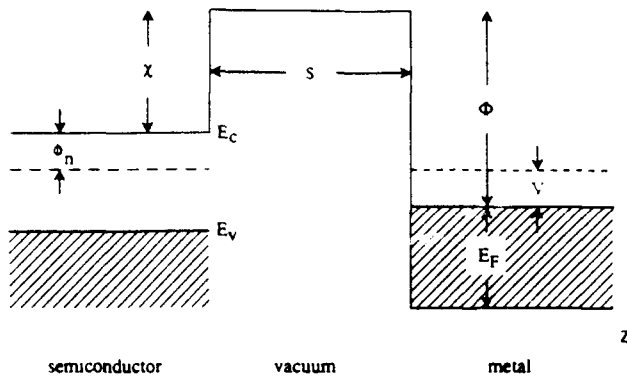


FIG. 1. Energy diagram for an ideal semiconductor-vacuum-metal junction, when the applied bias V has been chosen to eliminate any electric field arising from the difference in metal and semiconductor work functions, $\Phi - (\gamma + \phi_n)$. Here γ is the semiconductor electron affinity, and ϕ_n the offset of the Fermi level from the bottom of the conduction band.

well-known, however, that this potential diverges at the interfaces. The unphysical divergences may be circumvented using a Thomas-Fermi theory of dielectric screening.^{11,12} The Thomas-Fermi dielectric function in a bulk metal is $\epsilon_m(k) = 1 + \gamma_m^2/k^2$, where γ_m is the corresponding Thomas-Fermi wave vector. For a point charge q_0 located at position r_0 , the electrostatic potential inside the metal, $\phi_m(r, r_0)$, satisfies the equation

$$(\nabla^2 - \gamma_m^2)\phi_m(r, r_0) = -4\pi q_0 \delta(r - r_0). \quad (2)$$

Within the same approximation, the screening response of a bulk semiconductor to a point charge may be modeled using the dielectric function given by Inkson,¹¹

$$\epsilon_s(k) = 1 + [(\epsilon_s - 1)/(1 + \epsilon_s k^2/\gamma_s^2)], \quad (3)$$

where ϵ_s is the static dielectric constant and γ_s an effective Thomas-Fermi wave vector. It is easily shown that the electrostatic potential inside the semiconductor, $\phi_s(r, r_0)$, then satisfies the equation¹¹

$$(\nabla^2 - \gamma_s^2)\phi_s(r, r_0) = -(\gamma_s^2/\epsilon_s)u(r, r_0) - 4\pi(q_0/\epsilon_s)\delta(r - r_0), \quad (4)$$

where $u(r, r_0)$ is the vacuum potential, $q_0/|r - r_0|$. Equations (2) and (4) are just coordinate space representations of the fundamental linear relationship, $\phi_{m,s}(k) = u(k)/\epsilon_{m,s}(k)$.

In turning to the junction shown in Fig. 1, we assume the dielectric functions defined for bulk media are unaffected by the presence of any interfaces, so that Eqs. (2) and (4) remain valid throughout their respective medium. The semiclassical solution to the electrostatic potential inside the metal, ϕ_m , is then given by Eq. (2), subject to boundary conditions at the metal-vacuum interface. In order to determine the semiclassical expression for ϕ_s , however, we must specify the vacuum potential, u , in addition to boundary conditions at the semiconductor-vacuum interface. In evaluating u , we need to consider the contribution of all charge external to the semiconductor half space, in addition to any charge placed inside the medium. As a lowest order approximation, we add to u the vacuum potential from the external image charges which generate the correct classical solution

inside the semiconductor, and then determine ϕ_s from Eq. (4). With this choice for u , the resulting semiclassical potential, ϕ_s , naturally approaches the classical solution at distances greater than a few Thomas-Fermi wavelengths from the interface. To obtain the semiclassical image potential, one simply evaluates the semiclassical electrostatic potential at the position of the point charge, excluding the field produced by the charge itself.

Defining the quantities

$$\alpha_m(k) = \frac{k}{(k^2 + \gamma_m^2)^{1/2}}, \quad (5a)$$

$$\alpha_s(k) = \frac{k}{(k^2 + \gamma_s^2)^{1/2}}, \quad (5b)$$

$$\eta_m(k) = \frac{1 - \alpha_m(k)}{1 + \alpha_m(k)}, \quad (6a)$$

$$\eta_s(k) = \frac{1 - \alpha_s(k)}{1 + \alpha_s(k)}, \quad (6b)$$

we show in the Appendix that the semiclassical image potential felt by a point charge q_0 in the vacuum region, $0 < z_0 < s$, is

$$\varphi_v(z_0) = q_0 \int_0^\infty (B_k^v e^{kz_0} + C_k^v e^{-kz_0}) dk, \quad (7)$$

where

$$B_k^v = -\eta_m e^{-ks} \frac{\eta_s F_k^v/\epsilon_s - \eta_s e^{k(s-z_0)} + e^{k(s+z_0)}}{e^{2ks} - \eta_s \eta_m}, \quad (8)$$

$$C_k^v = \eta_s e^{ks} \frac{F_k^v/\epsilon_s - e^{k(s-z_0)} + \eta_m e^{-k(s-z_0)}}{e^{2ks} - \eta_s \eta_m}, \quad (9)$$

and

$$F_k^v = \epsilon_s(1 - \beta) \frac{e^{k(s-z_0)} - e^{-k(s-z_0)}}{1 - \beta e^{-2ks}}, \quad (10)$$

with

$$\beta = (\epsilon_s - 1)/(\epsilon_s + 1). \quad (11)$$

The corresponding potential energy, $V_{\text{image}}(z_0)$, is then given by $q_0 \varphi_v(z_0)/2$.

The image potential for q_0 in the semiconductor ($z_0 < 0$) is similarly found to be

$$\varphi_s(z_0) = \frac{q_0}{\epsilon_s} \int_0^\infty \{F_k^s e^{kz_0} + A_k^s \exp[(k^2 + \gamma_s^2)^{1/2} z_0]\} dk, \quad (12)$$

where

$$F_k^s = -\frac{e^{-2ks} - \beta}{1 - \beta e^{-2ks}} e^{kz_0}, \quad (13)$$

and

$$A_k^s = (2\alpha_s/(1 + \alpha_s))\{\eta_m e^{-k(2s-z_0)} + F_k^s\} + (\epsilon_s - 1) \times [\eta_m e^{-2ks} - \eta_s] \exp[(k^2 + \gamma_s^2)^{1/2} z_0] / (1 - \eta_s \eta_m e^{-2ks}). \quad (14)$$

Finally for q_n in the metal ($z_n > s$) we have

$$\varphi_m(z_n) = q_n \int_0^{\infty} \exp[(k^2 - \gamma_m^2)^{1/2}(s - z_n)] D^m dk, \quad (15)$$

with

$$D^m = \frac{\eta_m - \eta_e e^{-2\gamma_m s}}{1 - \eta_e \eta_m e^{-2\gamma_m s}} \exp[(k^2 - \gamma_m^2)^{1/2}(s - z_n)]. \quad (16)$$

It is easily verified that the expressions above reproduce the classical image potential in the limits $\gamma_{s,m} \rightarrow \infty$. If we consider instead the limit of very large gap spacing, $s \rightarrow \infty$, we recover the semiclassical result of Newns¹² for an isolated vacuum-metal interface, and an analogous result for the semiconductor-vacuum interface. In the limit of a vanishing vacuum gap, $s \rightarrow 0$, our junction reduces to a semiconductor-metal contact. In this case, the results derived above differ in detail from those quoted by Inkson¹¹ because of our different *ansatz* for $u(\mathbf{r}, r_0)$. In effect, Inkson treats the semiconductor-metal interface by constructing u from the solution for a classical dielectric in contact with a Thomas-Fermi metal. Our starting point for the same problem would be the solution to a classical dielectric in contact with a classical metal. If we introduce a vacuum gap between the two media, the distinction between these approaches becomes unimportant for separations s which are large compared with a Thomas-Fermi screening length in the metal.

The effective one-electron potential in the junction is obtained by adding the semiclassical image potential to the band diagram shown in Fig. 1. To clearly separate the image interaction from other factors which might influence the determination of an apparent barrier height,¹⁰ we presume the applied bias V has been chosen to eliminate the electric field between tip and sample in the absence of image corrections. Selecting the bottom of the semiconductor conduction band as our energy reference, the one-electron potential is then given by $\frac{1}{2}q_0\varphi_s$ in the semiconductor, $\frac{1}{2}q_0\varphi_v + \chi$ in the vacuum, and $\frac{1}{2}q_0\varphi_m + \chi - (\Phi + E_F)$ in the metal. This function, though finite, is discontinuous at the semiconductor-vacuum and vacuum-metal boundaries. It is unreasonable to expect our semiclassical treatment to be entirely accurate within a screening length of the interfaces for a variety of reasons. First, the treatment assumes bulk values for the screening parameters. Second, the correct behavior of the image potential across an interface can only be deduced by taking full account of many-body effects.¹³ Finally, there is no *a priori* relationship between the effective band bending we calculate in the immediate vicinity of the interfaces, and the one-electron potential we use to model band structure, which guarantees that the contribution from the surface dipole layer, together with exchange and correlation effects, will produce a smoothly varying total potential across the interface. Since we believe the effective one-electron potential should be continuous when all these effects are self-consistently accounted for, we have supplemented our picture by employing a third-order polynomial to smoothly join the potential and its derivative at points a distance $\gamma_{s,m}^{-1}$ from either side of the boundaries. We then use this interpolation to represent the tunneling potential within the interfacial

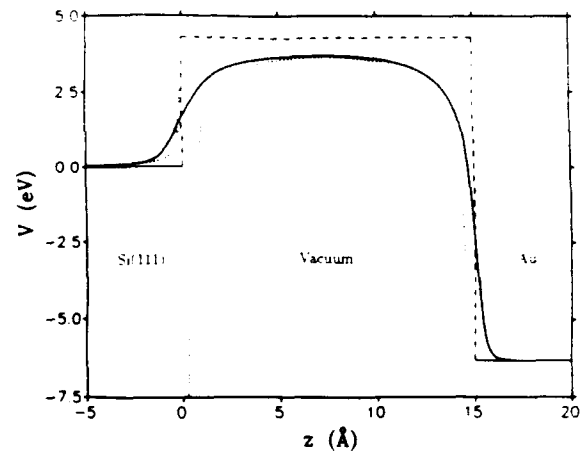


FIG. 2. Effective one-electron potential energy as a function of position. Solid line: including the semiclassical image potential with interpolation. Dotted line: including the classical image interaction. Dashed line: neglecting image effects. Here $\chi = 4.3$ eV, $\Phi = 5.1$ eV, and $E_F = 5.3$ eV.

layer. An example of this interpolated potential is presented in Fig. 2, where we contrast our results with the classical calculation, for a junction consisting of a *n*-type hydrogen-terminated Si(111) surface and gold tip electrode, with $\gamma_m = 1.7 \text{ \AA}^{-1}$, $\gamma_s = 1.16 \text{ \AA}^{-1}$, and $\epsilon_s = 11.9$.¹⁴⁻¹⁶

The method used in computing the tunneling current is the same as that described in Ref. 10. Briefly, the potential is substituted into a one-dimensional, effective mass Schrödinger equation, which is solved numerically to evaluate a transmission probability. Finite temperature supply functions are then employed to determine the current density.¹⁷ The apparent barrier as a function of gap spacing is calculated via Eq. (1), and our results illustrated in Fig. 3. The theoretical barrier height, defined by the maximum of the potential in the vacuum region, is also shown for comparison. As one sees from the figure, the image interaction reduces the theoretical barrier height with decreasing gap spacing, but the effect is significant only for s less than 10 Å. The apparent barrier height defined in Eq. (1), on the other

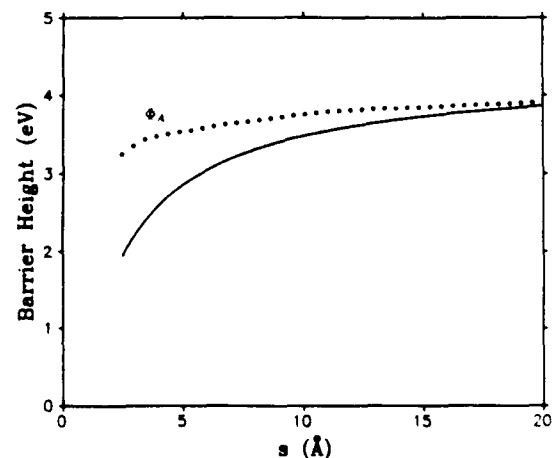


FIG. 3. Apparent (dotted line) and theoretical (solid line) barrier height vs electrode separation s for $T = 300$ K. The results are virtually independent of doping in the nondegenerate regime.

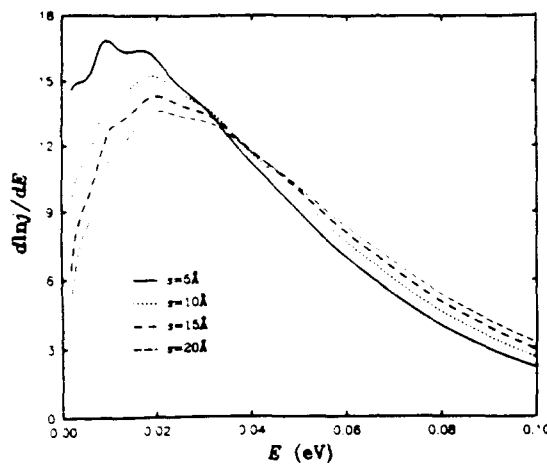


FIG. 4. Differential current density distribution vs normal energy at several tip-sample separations.

hand, never varies appreciably, and differs little from the electron affinity of the semiconductor. This is essentially equivalent to the result for a MVM tunneling junction.

The similarity in apparent barrier height as a function of gap spacing in MVS and MVM junctions suggests that the influence of image interactions on electron tunneling in the semiconductor is not significant. This appears contrary to expectations based on the long-range nature of the image force in a dielectric medium. Specifically, since tunneling electrons in a nondegenerate, *n*-type semiconductor originate from the bottom of the conduction band (see, for example, the calculated differential current density distributions shown in Fig. 4), one would argue that the tunneling current should be sensitive to variations in the precise form of this long-range potential with electrode separation. However, there is an interesting point whose importance is overlooked in prior classical treatments of this problem,^{8,9} but which is crucial to the discussion here: Near a semiconductor surface, the image potential is dominated by induced charge at the semiconductor-vacuum interface. The sign of this charge depends only on the discontinuity in polarizability at the interface and results in a repulsive force. At distances in the semiconductor interior which are large compared to the electrode spacing, however, the vacuum-metal interface also contributes to the induced charge determining the long-range potential. Since the polarizability of the metal exceeds that of the semiconductor, the net force is now attractive. Because the image force must vanish far from the semiconductor surface, at distances between these two extremes the image potential, and therefore the effective band bending, must change sign. Consequently, the induced tunneling barrier only extends to the point where the image potential passes through zero, and is thus of finite range. The effect of the remaining long-range attractive part of the image potential on electron tunneling may be seen in the resonance structure displayed by the differential current densities shown in Fig. 4. In the particular case considered here, the zero crossing is given by $z_0/s = 3.59$. For all of our calculations, we have truncated the effective one-dimensional potential on the semiconductor side of the junction at a distance which is large compared with z_0 , and presumed that Debye-Hückel

screening due to free carriers is insignificant on this length scale.

In conclusion, we have examined a model STM junction in which the only contribution to the tunneling barrier in the semiconductor is from the image potential. In this case the apparent barrier height is insensitive to electrode separation. The finite range of the image induced barrier in the semiconductor provides a natural explanation for this. As seen in Fig. 2, the total area contributed by the tunneling barrier in the semiconductor is typically small compared with that contributed by the vacuum gap. Furthermore, the small effective mass for electron tunneling along the (111) axes in silicon enhances the transparency of any barrier in this direction.¹⁰

Despite fundamental differences in the long-range screening properties of metals and semiconductors which suggest a more prominent role for the image potential in metal-vacuum-semiconductor versus metal-vacuum-metal tunneling, it appears that the experimentally determined barrier height in STM measurements will be equally insensitive to image effects in both instances. The physical origin of this insensitivity is different in the two cases, however, and, for the semiconductor, may be traced to the short-range nature of the tunneling barrier induced by the long-range image force in a dielectric medium near a metal electrode.

We thank J. Kramar for providing part of the computer codes on which this calculation is based, and A. Baratoff for helpful discussions. This work was supported by the Office of Naval Research through Grant Nos. N00014-89-J-3029 and N00014-91-J-1126, and by the Robert A. Welch Foundation.

APPENDIX

We first consider the case where a point charge q_0 is placed in the vacuum region of the junction shown in Fig. 1. The electrostatic potential in each of the three regions is determined by the equations

$$\begin{cases} (\nabla^2 - \gamma_s^2)\phi_s(\mathbf{r}, \mathbf{r}_0) = -(\gamma_s^2/\epsilon_s)u(\mathbf{r}, \mathbf{r}_0), & z < 0 \text{ (semiconductor)} \\ \nabla^2\phi_v(\mathbf{r}, \mathbf{r}_0) = -4\pi q_0\delta(\mathbf{r} - \mathbf{r}_0), & 0 < z < s \text{ (vacuum)} \\ (\nabla^2 - \gamma_m^2)\phi_m(\mathbf{r}, \mathbf{r}_0) = 0, & z > s \text{ (metal)} \end{cases} \quad (\text{A1})$$

where $\mathbf{r}_0 = (0, 0, z_0)$ is the position of q_0 . The general solution to these equations subject to the boundary condition that both ϕ_s and ϕ_m vanish at ∞ , may be expressed in cylindrical coordinates as follows:

$$\begin{aligned} \phi_s(\mathbf{r}, \mathbf{r}_0) = & \frac{q_0}{\epsilon_s} \int_0^\infty F_k^s J_0(k\rho) e^{k(z-z_0)} dk + \frac{q_0}{\epsilon_s} \\ & \times \int_0^\infty A_k^s J_0(k\rho) \exp[(k^2 + \gamma_s^2)^{1/2} z] dk, \end{aligned} \quad (\text{A2})$$

$$\begin{aligned} \phi_m(\mathbf{r}, \mathbf{r}_0) = & q_0 \int_0^\infty J_0(k\rho) (e^{-k(z-z_0)} \\ & + B_k^m e^{kz} + C_k^m e^{-kz}) dk, \end{aligned} \quad (\text{A3})$$

and

$$\phi_m(\mathbf{r}, \mathbf{r}_0) = q_0 \int_0^\infty D_k^m J_0(k\rho) \exp[-(k^2 + \gamma_m^2)^{1/2} z] dk. \tag{A4}$$

The first term in Eq. (A2) is the particular solution $u(\mathbf{r}, \mathbf{r}_0)/\epsilon_1$, where we have approximated u using the well-known classical expression^{8,9} given in Eq. (10). The second term is a homogeneous solution arising from short range screening in the semiconductor. Equation (A3) for ϕ_v contains a particular solution due to the point charge q_0 , as well as a homogeneous solution. The coefficients A_k^v , B_k^v , C_k^v , and D_k^v are determined by four boundary conditions at the interfaces, namely

$$\phi_v|_{z=0} = \phi_m|_{z=0}, \tag{A5}$$

$$\frac{\partial \phi_v}{\partial z} \Big|_{z=0} = \frac{\partial \phi_m}{\partial z} \Big|_{z=0}, \tag{A6}$$

$$\phi_v|_{z=s} = \phi_m|_{z=s}, \tag{A7}$$

and

$$\frac{\partial \phi_v}{\partial z} \Big|_{z=s} = \frac{\partial \phi_m}{\partial z} \Big|_{z=s}. \tag{A8}$$

In imposing continuity of the electrostatic potential and its derivative at these boundaries, we make the physical assumption that all interfacial charge is distributed over a finite width. Since we exclude an abrupt surface charge, the factor ϵ which normally accompanies the classical continuity equation for $\partial\phi/dz$ no longer appears in our boundary conditions for the semiclassical solution.

The image potential is obtained from ϕ_v by setting $\mathbf{r} = \mathbf{r}_0$ and excluding the self-energy term. The resulting expression is given by Eqs. (7)-(11).

When q_0 is in the semiconductor, the regional differential equations become

$$\begin{cases} (\nabla^2 - \gamma_1^2)\phi_v(\mathbf{r}, \mathbf{r}_0) = -(\gamma_1^2/\epsilon_1)u(\mathbf{r}, \mathbf{r}_0) \\ \quad - 4\pi q_0 \delta(\mathbf{r} - \mathbf{r}_0), \\ \quad \quad \quad z < 0 \text{ (semiconductor);} \\ \nabla^2 \phi_v(\mathbf{r}, \mathbf{r}_0) = 0, \\ \quad \quad \quad 0 < z < s \text{ (vacuum);} \\ (\nabla^2 - \gamma_m^2)\phi_m(\mathbf{r}, \mathbf{r}_0) = 0, \\ \quad \quad \quad z > s \text{ (metal)} \end{cases} \tag{A9}$$

The solutions in these three regions are

$$\begin{aligned} \phi_v(\mathbf{r}, \mathbf{r}_0) = & \frac{q_0}{\epsilon_1} \int_0^\infty J_0(k\rho) e^{kz - z_0} dk + q_0 \frac{\epsilon_1 - 1}{\epsilon_1} \\ & \times \int_0^\infty J_0(k\rho) \exp[(k^2 + \gamma_1^2)^{1/2} z - z_0] dk \\ & + \frac{q_0}{\epsilon_1} \int_0^\infty F_k^v J_0(k\rho) e^{kz} dk + \frac{q_0}{\epsilon_1} \\ & \times \int_0^\infty A_k^v J_0(k\rho) \exp[(k^2 + \gamma_1^2)^{1/2} z] dk, \end{aligned} \tag{A10}$$

$$\phi_m(\mathbf{r}, \mathbf{r}_0) = q_0 \int_0^\infty J_0(k\rho) (B_k^m e^{kz} + C_k^m e^{-kz}) dk, \tag{A11}$$

and

$$\phi_m(\mathbf{r}, \mathbf{r}_0) = q_0 \int_0^\infty D_k^m J_0(k\rho) \exp[-(k^2 + \gamma_m^2)^{1/2} z] dk. \tag{A12}$$

Additional inhomogeneous terms now arise in Eq. (A10) from the presence of the point charge in the semiconductor.¹¹ The classical expression^{8,9} is again used to represent the vacuum potential u and the resulting image potential is given by Eqs. (12)-(14).

Finally, when q_0 is in the metal, we have

$$\begin{cases} (\nabla^2 - \gamma_1^2)\phi_v(\mathbf{r}, \mathbf{r}_0) = -(\gamma_1^2/\epsilon_1)u(\mathbf{r}, \mathbf{r}_0), \\ \quad \quad \quad z < 0 \text{ (semiconductor);} \\ \nabla^2 \phi_v(\mathbf{r}, \mathbf{r}_0) = 0, \\ \quad \quad \quad 0 < z < s \text{ (vacuum);} \\ (\nabla^2 - \gamma_m^2)\phi_m(\mathbf{r}, \mathbf{r}_0) = -4\pi q_0 \delta(\mathbf{r} - \mathbf{r}_0), \\ \quad \quad \quad z > s \text{ (metal).} \end{cases} \tag{A13}$$

whose general solutions are

$$\begin{aligned} \phi_v(\mathbf{r}, \mathbf{r}_0) = & \frac{q_0}{\epsilon_1} \int_0^\infty F_k^v J_0(k\rho) e^{kz} dk + \frac{q_0}{\epsilon_1} \\ & \times \int_0^\infty A_k^v J_0(k\rho) \exp[(k^2 + \gamma_1^2)^{1/2} z] dk, \end{aligned} \tag{A14}$$

$$\phi_m(\mathbf{r}, \mathbf{r}_0) = q_0 \int_0^\infty J_0(k\rho) (B_k^m e^{kz} + C_k^m e^{-kz}), \tag{A15}$$

and

$$\begin{aligned} \phi_m(\mathbf{r}, \mathbf{r}_0) = & q_0 \int_0^\infty J_0(k\rho) \\ & \times \exp[-(k^2 + \gamma_m^2)^{1/2} z - z_0] dk \\ & + q_0 \int_0^\infty D_k^m J_0(k\rho) \\ & \times \exp[-(k^2 + \gamma_m^2)^{1/2} z] dk. \end{aligned} \tag{A16}$$

Here we have assumed the vacuum potential u vanishes in the semiconductor, as it must in the classical case where the metal completely screens the point charge. Similar derivations then result in Eqs. (15) and (16).

¹J. G. Simmons, *J. Appl. Phys.* **34**, 1793 (1963).
²H. Q. Nguyen, T. E. Feuchtwang, and P. H. Cutler, *J. Phys.* **47**, C2 (1986).
³N. D. Lang, *Phys. Rev. B* **37**, 10395 (1988).
⁴G. Binnig, N. Garcia, H. Rohrer, J. M. Soler, and F. Flores, *Phys. Rev. B* **30**, 4816 (1984).
⁵G. Binnig, H. Rohrer, Ch. Gerber, and E. Weibel, *Appl. Phys. Lett.* **40**, 178 (1982).
⁶J. H. Coombs, M. E. Welland, and J. B. Pethica, *Surf. Sci.* **198**, L353 (1988).
⁷For treatments in nonplanar geometries see, for example, A. A. Lucas *et al.*, *J. Phys.* **45**, C9 (1984); H. Morawitz *et al.*, *Surf. Sci.* **180**, 333 (1987); J. Mahanty and M. T. Michalewicz, *Austral. J. Phys.* **40**, 413 (1987).
⁸M. Kleefstra and G. C. Herman, *J. Appl. Phys.* **51**, 4923 (1980).
⁹A. Tugulea and D. Dascalu, *J. Appl. Phys.* **56**, 2823 (1984).
¹⁰M. Weimer, J. Kramar, and J. D. Baldeschwieler, *Phys. Rev. B* **39**, 5572 (1989).

- ¹J. C. Inkson, *J. Phys. C* **4**, 591 (1971).
- ²D. M. Newns, *J. Chem. Phys.* **50**, 4572 (1969).
- ³D. Lang, *Solid State Phys.* **28**, 225 (1973).
- ⁴N. W. Ashcroft and N. D. Mermin, *Solid State Physics* (Holt, New York, 1976).
- ⁵J. P. Walter and M. L. Cohen, *Phys. Rev. B* **2**, 1821 (1970).
- ⁶S. M. Sze, *Physics of Semiconductor Devices* (Wiley, New York, 1961).
- ⁷The doping density n is essentially irrelevant to the calculation presented here, since the only quantity which depends on n is the position of the semiconductor Fermi level. In the nondegenerate case this merely affects the overall normalization of the supply functions.

Internal Image Potential in Semiconductors: Effect on Scanning Tunneling Microscopy

Z.-H. Huang, M. Weimer, and R. E. Allen
Department of Physics, Texas A&M University
College Station, TX 77843-4242

Abstract

The tunneling of electrons from a semiconductor surface to a metal tip, across a vacuum gap, is influenced by two image interactions: an attractive image potential in the vacuum region, which lowers the apparent tunneling barrier, and a repulsive image potential in the semiconductor interior, which raises it for conduction band electrons. We report on detailed calculations of tunneling currents and apparent barrier heights for a model metal-vacuum-semiconductor junction which utilizes semiclassical dielectric functions to compute the image potential in all three regions. The effect of image forces is found to be small compared to that of either the vacuum barrier or tip-induced band bending. In particular, the image-induced barrier in the semiconductor has only a minor influence on either the apparent barrier height or the shape of current-voltage characteristics, both of which are routinely measured in STM experiments. This finding is explained by a qualitative WKB analysis and several simple arguments.

I. Introduction

Electron tunneling through a junction is often treated by considering independent electrons moving in an effective potential. The simplest model potential for a metal-vacuum-metal (MVM) junction is the rectangular barrier, but it is well known that image forces modify this potential significantly. Calculations based on classical electrostatics, for example, reveal that the image interaction reduces the effective vacuum barrier by lowering its maximum height and slightly narrowing its width [1-3]. More realistic quantum mechanical calculations employing the density functional formalism indicate that the lowest order correction to this classical picture is simply a displacement of the effective image plane by several tenths of an angstrom, along with a smooth matching of the vacuum potential outside the surface to the minimum of the conduction band in the metal interior [4,5]. The resulting vacuum barrier height now depends on the gap spacing s , and is well approximated by [6]

$$\Phi(s) = \Phi_0 - \frac{\alpha}{s - s_0}, \quad (1)$$

where Φ_0 represents the average work function of the metal electrodes, s_0 accounts for the shift in image plane positions, and $\alpha \sim 10 \text{ eV \AA}$.

The scanning tunneling microscope (STM), with which one can precisely adjust s , and hence continuously vary the vacuum barrier, is a potentially valuable tool for investigating this effect. By modulating the distance between tip and sample at a frequency outside the microscope's feedback bandwidth, and detecting a synchronous ac tunnel current, one can infer an apparent barrier height [7] according to

$$\Phi_A = [(-1/A)d \ln I / ds]^2, \quad (2)$$

where $A = 1.025 \text{ eV}^{-1/2} \text{ \AA}^{-1}$. The utility of (2) stems both from the fact that it is an experimentally accessible quantity, and that in a Wentzel-Kramers-Brillouin (WKB) approximation for the rectangular barrier it yields the correct barrier height. Early experiments on metals, however, revealed no discernible reduction in Φ_A by image forces at separations of more than a few angstroms. This insensitivity, it was argued [6], is due not to the absence of image effects, but, rather, to the particular form of the potential in (1), for which a WKB analysis shows that the first order term in an expansion of Φ_A in powers of s^{-1} vanishes. Other lines of reasoning similarly supported the conclusion that the apparent barrier height (2) is unlikely to be a sensitive probe of the image potential in MVM tunneling at large distances [8]. Nevertheless, the question of image

effects and their relevance to STM experiments continues to hold great interest. Subsequent investigators have addressed a number of fundamental issues, including the role of non-planar geometry [9-12], the precise nature of the effective vacuum barrier at short distances [7,13,14], and the influence of the dynamic image interaction in time-dependent tunneling [15].

If we replace one of the metal electrodes by a semiconductor to form a metal-vacuum-semiconductor (MVS) junction, then the image correction to the vacuum potential at large distances will be similar to that of the MVM junction when scaled to reflect the dielectric behavior of the semiconductor [16]. A qualitatively new phenomenon now appears, however, in that tunneling electrons experience an additional image force in the semiconductor interior due to the finite polarizability of that medium. In a classical multiple-image analysis of the planar MVS or SVS junction, this "internal" image potential is given by the expression [17,18]

$$V_s(z) = \frac{q^2}{16\pi\epsilon_s} \sum_{n=0}^{\infty} (\beta\beta')^n \left(\frac{\beta}{ns-z} - \frac{\beta'}{(n+1)s-z} \right), \quad (3)$$

for an extra point charge q located at $z < 0$, with $z = 0$ the position of the semiconductor-vacuum interface, and $z = s$ the position of the vacuum-metal interface. Here, ϵ_s is the static dielectric permittivity of the semiconductor and

$$\beta = \frac{(\epsilon_s - \epsilon_0)}{(\epsilon_s + \epsilon_0)}, \quad (4)$$

with a corresponding expression for β' . For an MVS junction, $\beta' = 1$. The internal image potential (3) leads to an effective increase in the semiconductor band gap near an ideal semiconductor-vacuum interface, since electrons in the conduction band are repelled from the surface whereas electrons in the valence band are attracted [17]. Image-induced features of this kind have, in fact, recently been proposed as an explanation for the thickness-dependent energy shifts observed in both XPS and AES spectra of thin SiO₂ films on silicon substrates [19]. The situation is exactly reversed at an ideal semiconductor-metal interface where the band gap is effectively decreased, a phenomenon already anticipated from the quantum many-body point of view [20].

To explicitly show the functional dependence on gap spacing, equation (3) may be written in scaled form [18] as

$$V_s(z) = \frac{q^2}{8\pi\epsilon_0 s} U_s(\beta, \beta', \xi), \quad (5)$$

where $\xi = z/s$ and U_s is a dimensionless function independent of s . In an MVS junction, $V_s(z)$ changes sign at a position $z_0 = s\xi_0(\beta)$ because the contribution from polarization charge at the metal-vacuum interface eventually dominates that of the semiconductor-vacuum interface deep in the semiconductor interior. Thus, a conduction band electron approaching the surface will experience an image interaction which is at first attractive, and then repulsive, with

$$\begin{aligned} U_s < 0, \xi < \xi_0(\beta) \\ U_s = 0, \xi = \xi_0(\beta) \\ U_s > 0, \xi > \xi_0(\beta) \end{aligned} \quad (6)$$

The image induced tunneling barrier in the semiconductor is then strongly dependent on electrode separation. It is appealing, therefore, to examine the possibility of detecting this additional barrier using the scanning tunneling microscope.

The classical expression for the image potential is inconvenient to use in tunneling calculations implementing transfer matrix methods, since it diverges at the interfaces, where unphysical bound states may be introduced. A semiclassical theory for the MVS junction which removes these divergences, but nevertheless requires an interpolation for the total effective potential in the near interfacial region, has recently been discussed^[21]. Initial calculations based on this theory showed that, for the special case of vanishing electric field between tip and sample, the contribution to Φ_A from the image induced barrier in the semiconductor is small. The insensitivity of Φ_A to this additional correction, it was argued, could be ascribed to the short-range nature of the induced barrier in the semiconductor, which therefore appears nearly transparent. It is the purpose of this paper to re-examine the question of observing such image effects in an MVS junction under more general circumstances.

To do so, we first review briefly the phenomenology of apparent barrier heights in tunneling experiments at unpinned semiconductor surfaces. At zero applied bias there will, in general, be a space charge induced in the semiconductor by the difference between tip and sample work functions, $\Delta\Phi = \Phi - (\chi + \phi_n)$, as shown in Fig 1(a) for n -type material in depletion. This space charge may be eliminated only by applying an appropriate bias voltage, $V_{FB} = -\Delta\Phi$, to recover the flat-band condition illustrated in Fig. 1(b). Tip-induced band bending of the kind indicated in Fig.

1(a) will dramatically affect STM measurements of Φ_A , for reasons which are easy to appreciate [22]. The surface potential V_d is a monotonically decreasing function of s , with a maximum at $s = 0$. Since the depletion width W is typically much longer than s , only those carriers with a thermally activated kinetic energy greater than V_d will surmount the diffusion barrier to arrive at the semiconductor-vacuum interface. Increasing the separation between tip and sample exponentially suppresses tunneling through the vacuum barrier as before, but now also exponentially enhances the number of electrons reaching the semiconductor surface. Because of these two competing factors, the observed variation in current density is less than expected; this is then interpreted as a smaller barrier height in Eq. (2). If the image-induced potential (5) is superimposed on the space charge potential of Fig 1(a), it too will change with gap spacing. Since the energy scale characterizing the carrier distribution is kT , we may now ask whether inclusion of the semiconductor image potential further perturbs the carrier distribution, and thus the logarithmic derivative of the tunneling current, in any measurable way.

In what follows, we first present key elements of the semiclassical image potential theory, and describe our method of calculation, in Section II. Predictions for the apparent barrier height and tunneling current-voltage characteristics, including image effects, are presented in Section III for the particular case of a planar, n -type hydrogen-passivated Si (111)/Au junction. We devote Section IV to a qualitative discussion of these results within the framework of a WKB analysis, which permits us to generalize our findings beyond the specific materials we have chosen to study in detail. Section V summarizes our conclusions.

II. Description of the Calculation

Our calculations are carried out under the assumption that the system consists of independent electrons moving in an effective one-dimensional potential. The bulk metal is treated as a free-electron Fermi gas characterized by Fermi energy E_F and work function Φ . The semiconductor is modeled in a one-band effective-mass approximation including anisotropy. When assembled into an MVS junction, the semiconductor-vacuum and vacuum-metal interfaces perturb these bulk effective potentials; the corrections we specifically consider here are introduced by the multiple-image interaction and tip-induced space charges. Modifications due to surface states or collective surface excitations are ignored.

The expressions for the classical image potential in an ideal metal-insulator-semiconductor (MIS) junction similar to that shown in Fig. 1 diverge at the semiconductor-vacuum and vacuum-metal interfaces [17,18]. These unphysical divergences may be circumvented by employing an effective

Thomas-Fermi theory of dielectric screening ^[23,24] to derive a semiclassical expression for the image potential experienced by a tunneling electron. Specifically, the Thomas-Fermi dielectric function in a bulk metal is given by $(\epsilon_m(k) / \epsilon_0) = (1 + \gamma_m^2 / k^2)$, where γ_m is the corresponding Thomas-Fermi wave vector. Within the same approximation, the screening response of an intrinsic bulk semiconductor may be modeled by the dielectric function ^[23]

$$(\epsilon_s(k) / \epsilon_0) = 1 + \frac{(\epsilon_s / \epsilon_0) - 1}{1 + (\epsilon_s / \epsilon_0)(k^2 / \gamma_s^2)}, \quad (7)$$

where $(\epsilon_s / \epsilon_0)$ is the long-wavelength static dielectric constant and γ_s an effective Thomas-Fermi wave vector which depends on the total valence charge density. It can then be shown ^[21] that the resulting semiclassical expression for the image potential experienced by a point charge q located at position $z < 0$ in the semiconductor is

$$V_s(z) = \frac{q^2}{8\pi\epsilon_s} \int_0^\infty \left\{ F_k^s e^{kz} + A_k^s \exp\left[(k^2 + \gamma_s^2)^{1/2} z\right] \right\} dk, \quad (8)$$

where

$$F_k^s = -\frac{e^{-2ks} - \beta}{1 - \beta e^{-2ks}} e^{kz}, \quad (9)$$

coincides with the classical solution ^[17,18] and

$$A_k^s = -\frac{\left\{ \frac{2\alpha_s}{1 + \alpha_s} \right\} (\eta_m e^{-k(2s-z)} + F_k^s) + \left\{ \frac{2\beta}{1 - \beta} \right\} (\eta_m e^{-2ks} - \eta_s) \exp\left[(k^2 + \gamma_s^2)^{1/2} z\right]}{1 - \eta_s \eta_m e^{-2ks}}, \quad (10)$$

represents an additional response arising from short-range screening in the semiconductor. Here, we define, in addition to β in (4) above,

$$\alpha_m(k) = \frac{k}{(k^2 + \gamma_m^2)^{1/2}}, \quad (11)$$

$$\alpha_s(k) = \frac{k}{(k^2 + \gamma_s^2)^{1/2}}, \quad (12)$$

$$\eta_m(k) = \frac{1 - \alpha_m(k)}{1 + \alpha_m(k)}, \quad (13)$$

$$\eta_s(k) = \frac{1 - \alpha_s(k)}{1 + \alpha_s(k)}. \quad (14)$$

When q is located in the vacuum region $0 < z < s$, the corresponding expression for the semiclassical image potential becomes

$$V_v(z) = \frac{q^2}{8\pi\epsilon_0} \int_0^\infty (B_k^v e^{kz} + C_k^v e^{-kz}) dk, \quad (15)$$

where

$$B_k^v = -\eta_m e^{-kz} \frac{\left\{ \frac{1-\beta}{1+\beta} \right\} \eta_s F_k^v - \eta_s e^{k(s-z)} + e^{k(s+z)}}{e^{2kz} - \eta_s \eta_m}, \quad (16)$$

$$C_k^v = \eta_s e^{kz} \frac{\left\{ \frac{1-\beta}{1+\beta} \right\} F_k^v - e^{k(s-z)} + \eta_m e^{-k(s-z)}}{e^{2kz} - \eta_s \eta_m}, \quad (17)$$

and

$$F_k^v = (1 + \beta) \frac{e^{k(s-z)} - e^{-k(s-z)}}{1 - \beta e^{-2kz}}. \quad (18)$$

Finally, for q in the metal ($z > s$) one finds

$$V_m(z) = \frac{q^2}{8\pi\epsilon_0} \int_0^\infty \exp\left[(k^2 + \gamma_m^2)^{1/2} (s-z)\right] D_k^m dk, \quad (19)$$

with

$$D_k^m = \frac{\eta_m - \eta_s e^{-2kz}}{1 - \eta_s \eta_m e^{-2kz}} \exp\left[(k^2 + \gamma_m^2)^{1/2} (s-z)\right] \quad (20)$$

representing the effect of short-range screening. It is easily verified that the formulae for $V_s(z)$, $V_v(z)$, and $V_m(z)$ given above reproduce the expected classical results in the limits $\gamma_{s,m} \rightarrow \infty$, and that $V_m(z)$, in particular, vanishes.

An effective one-electron potential is obtained throughout the junction by adding the appropriate regional solution for the semiclassical image potential to the band diagram shown in Fig. 1. We first consider the case illustrated in Fig. 1(b) when the applied bias V_{FB} has been chosen to eliminate any electric field between tip and sample in the absence of image corrections. Selecting the bottom of the semiconductor conduction band as an energy reference, the one-electron potential is then given by $V_s(z)$ in the semiconductor, $V_v(z) + \chi$ in the vacuum gap, and $V_m(z) + \chi - (\Phi + E_F)$ in the metal. This function, though finite, is still discontinuous at the semiconductor-vacuum and vacuum-metal boundaries. There are a number of reasons for this discontinuity, which originates from inadequacies in the semiclassical treatment at distances within a screening length of the interfaces. First, the treatment assumes bulk values for the screening parameters in each medium. Second, the correct behavior of the total effective potential (or self energy) experienced by an electron moving from inside a polarizable medium to the region immediately outside it, can only be deduced by taking full account of many-body effects^[4,5]. Finally, there is no *a priori* relationship between the effective band bending produced by image effects in the immediate vicinity of an interface, and the one-electron potential used to model band structure, which guarantees that the contribution from surface dipole layers, together with exchange and correlation effects, will produce a smoothly varying total potential across the interfaces. Since the true one-electron potential is presumably continuous when all of these effects are self-consistently accounted for, we supplement the semiclassical picture by employing a third-order polynomial to smoothly join the calculated potential and its derivative at points a distance $\gamma_{s,m}^{-1}$ on either side of the semiconductor-vacuum and vacuum-metal boundaries. This interpolation is then used to represent the tunneling potential in the near-interfacial regions. An example of this interpolated potential is presented in Fig. 2(a) for a junction consisting of a *n*-type hydrogen-terminated Si(111) surface and a gold tip electrode (with $\gamma_m=1.7\text{\AA}^{-1}$, $\gamma_s=1.16\text{\AA}^{-1}$, and $\epsilon_s=11.9$ ^[25-27]), where we contrast our results with the classical calculation.

The more general situation occurs when $V \neq V_{FB}$, and there is a non-vanishing field in the vacuum region. In the absence of surface states this field penetrates the semiconductor interior, and the resultant band bending due to the tip-induced space charge is schematically illustrated in Fig. 1(a) for *n*-type material when $\Delta\Phi = \Phi - (\chi + \phi_n) > 0$. The surface potential qV_d is a sensitive function of both gap spacing and bias voltage, and is given in the depletion approximation by^[22]

$$qV_d(s, V) = \Delta\Phi \left\{ \left[1 + (s/s_0)^2 + qV/\Delta\Phi \right]^{1/2} - s/s_0 \right\}^2. \quad (21)$$

The resulting electrostatic potential in the semiconductor interior, $\psi(z)$, has finite range, vanishing at $z = -W$, and follows the well-known form [27]

$$\psi(z) = V_d(1 + z/W)^2, \quad (22)$$

for $-W < z < 0$. The depletion width W is a function of both the bulk donor density N_d and the semiconductor surface potential qV_d through

$$W(qV_d) = (2\epsilon_s V_d / qN_d)^{1/2}, \quad (23)$$

while the length scale s_0 is obtained from the zero-bias, zero-separation depletion width according to [22]

$$s_0 = (\epsilon_0 / \epsilon_s) W(\Delta\Phi). \quad (24)$$

The total one-electron potential now includes a contribution from $\psi(z)$ as well as that from $V_s(z)$ for $z < 0$. As above, we interpolate within the near-interfacial region to obtain a continuous result as a function of position, and an example calculated for the same hydrogen-terminated Si(111)/Au junction, at a sample bias of -100 mV with $N_d = 5 \times 10^{17} \text{ cm}^{-3}$, is illustrated in Fig. 2(b), where the additional long-range effect of Debye screening due to free carriers has been ignored.

To compute a tunneling current density, the appropriate potential is substituted into a one-dimensional effective-mass Schrödinger equation for electrons originating from the conduction band of the semiconductor. This equation is then solved numerically to evaluate a transmission probability $D(E_z, s)$, where E_z is the energy component normal to the barrier. The net tunneling current density is then given by the expression

$$j(s) = \frac{em_t}{\gamma^{1/2} m_0} \int_0^\infty dE_z D(E_z, s) [N_0(E_z) - N_0(E_z - qV)], \quad (25)$$

where N_0 is the one-dimensional supply function for electrons at finite temperature in the semiconductor and metal, respectively, while γ represents an anisotropy factor for the constant energy surfaces of the six equivalent Si<100> ellipsoidal pockets at the indirect conduction band

minimum projected along the (111) direction. The resulting effective mass for tunneling in the (111) direction is $m_z^* = \gamma m_l = 0.26m_0$. Further details concerning the calculation of $D(E_z, s)$ may be found in Ref. [22].

III. Results

The tunneling current density as a function of gap spacing calculated on the basis of Eq. (25), using the one-electron effective potential of Fig. 2(b), is presented in Fig. 3 for a representative bias voltage which produces substantial majority carrier depletion in the near surface region of the semiconductor. For comparison, the results obtained using the potential of Fig. 1(a), neglecting image effects, are also shown. At each of the doping levels considered, we see roughly an order of magnitude increase in the overall current density at any reasonable gap separation due to the inclusion of image forces. The shape of the $j - s$ curves on a semi-logarithmic plot deviates at small s from the straight line predicted for vacuum tunneling because of the influence of tip-induced space charge on current transport through the junction, as explained previously [22]. What we wish to call attention to here is that the $j - s$ characteristics for a given doping display a similar *shape* whether or not image effects are included.

This observation is more quantitatively expressed in Fig. 4, where an apparent barrier height as a function of gap spacing is obtained via Eq. (1) from the curves in Fig. 3. We see that the barrier height displays nearly the same behavior as a function of s (for a given doping) with or without image forces, but that including image effects results in an overall lowering of the apparent barrier by a few tenths of an eV. Also presented in Fig. 4 are the doping-independent results for Φ_A when the applied bias has been chosen to eliminate any tip-induced band bending [21], as shown in Fig. 1(b). It is clear from the figure that the principal influence on Φ_A arises from tip-induced space charge, and that the image potential constitutes a relatively small perturbation.

The influence of image forces on the tunneling current-voltage characteristics at constant separation may be calculated in a manner similar to the $j - s$ characteristics presented above, and the results are shown in Fig. 5, as a function of doping, for $s = 5\text{\AA}$. To facilitate a comparison between $j - V$ curves calculated with and without image corrections at fixed doping, and between $j - V$ curves obtained for different doping levels, both the current density and applied bias have been scaled to their respective flat band values. As already noted, the image potential increases the current density for a given applied bias and electrode separation, but we see here that the overall *shape* of the $j - V$ characteristic remains essentially unchanged. This shape is, again, dominated by the tip-induced

space charge. A discussion of the somewhat unusual properties of the reverse-bias characteristics may be found in the literature [28,29].

IV. Discussion

Our results for the specific case of a planar, passivated n -type Si (111)/Au junction indicate that the influence of image effects on the apparent barrier height is small, and may not be experimentally detectable in practice. The role of tip-induced space charge in determining the apparent barrier decreases with increasing bias as flat band conditions are approached [22], so that image effects, if detectable, will be most prominent at bias voltages very near V_{FB} . The shape of the tunneling current-voltage characteristics also appears to be insensitive to image forces.

In what follows, we examine these conclusions from the perspective of a WKB analysis of tunneling through the compound barrier created either by the space charge in the semiconductor neglecting image effects, followed by the vacuum gap, or the image potential in the semiconductor neglecting space charge, and the vacuum gap. In this way we can identify important qualitative features of the realistic junction problem containing both elements which will give us some insight into the relevance of specific material parameters to our results, and the circumstances under which image effects might play a more significant role.

The simplest case arises when the only barrier which need be considered is due to the vacuum gap. If we denote by $D^{vac}(E_z, s)$ the energy-dependent transmission coefficient, then in the WKB approximation one obtains

$$\ln D^{vac}(E_z, s) = -2(2m_0 / \hbar^2)^{1/2} (\chi - E_z)^{1/2} s. \quad (26)$$

The differential current density per unit energy at energy E_z is then

$$\partial j(E_z, s) / \partial E_z = D^{vac}(E_z, s) [N_0(E_z) - N_0(E_z - qV)], \quad (27)$$

and the condition for an extremum in this quantity is simply

$$-(1/kT) + \partial \ln D^{vac}(E_z, s) / \partial E_z \Big|_{E_z = E_m} = 0. \quad (28)$$

This condition, when appropriated generalized, gives Eq. (29) and is relevant to the discussion following (31). However, in the present case, the extremum in (28) turns out to be a local minimum, and a maximum is found at the end point $E_m = 0$. If the differential current density at this maximum is used to characterize the integrated tunneling current, Eq. (2) yields $\Phi_A = \chi$ for the apparent barrier height.

The next situation which is straightforward to analyze arises when we consider the effect of semiconductor space charge and ignore the vacuum barrier. This corresponds to the problem of tunneling through an ideal Schottky barrier structure. In this case, a WKB analysis reveals that the peak of the differential current distribution occurs at an energy ^[30,31]

$$E_m / V_d = \left\{ \cosh \left[q(\hbar^2 N_d / 4m_s \epsilon_s)^{1/2} / kT \right] \right\}^{-2}. \quad (29)$$

In the limit of low doping and long depletion widths, this ratio approaches unity, so that the differential current density is proportional to $e^{-V_d/kT}$ and one recovers the thermionic emission picture of current transport across a Schottky barrier ^[29].

The combined effect of the semiconductor space charge and a vacuum barrier is more difficult to follow through completely, but the qualitative features are apparent in at least one important limit. As noted in connection with Eq. (21), the semiconductor surface potential is a function of the vacuum gap width s . If one considers the physically realistic circumstance of $s/s_0 \ll 1$, which corresponds to electrode separations that are small compared to the sample depletion width, the energy distribution will be almost completely determined by the semiconductor space charge. A specific example, based on the more accurate calculations described in Section II, is presented in Fig. 6, where we see that E_m/V_d is nearly one, independent of s . Thus, for low doping, current transport is once again well-described by a thermionic emission picture, and one finds from Eq. (2) that ^[22]

$$\Phi_A^{1/2} = \chi^{1/2} + (1/A)(q/kT)[\partial V_d / \partial s]. \quad (30)$$

Since the surface potential decreases with increasing separation, s , the second term in (30) is opposite in sign to the vacuum barrier contribution. The distance dependence of V_d then has a profound influence on the apparent barrier height through its effect on the tunneling energy distribution.

Finally, we turn to the question of image forces and consider the case where we can neglect tip-induced band bending. A key issue is the extent to which image effects in the semiconductor interior perturb the energy distribution of tunneling electrons relative to that characteristic of the vacuum barrier alone. Ignoring image corrections in the vacuum region for simplicity, the extremum condition of Eq. (28) now becomes,

$$-(1/kT) + \partial \ln D^{\text{vac}}(E_i, s) / \partial E_i \Big|_{E_i = E_m} + \partial \ln D^{\text{semicond}}(E_i, s) / \partial E_i \Big|_{E_i = E_m} = 0, \quad (31)$$

which includes a contribution from the image-induced barrier in the semiconductor. A useful estimate of the last term in (31) is provided by considering the limit of infinite separation between tip and sample. The semiconductor barrier is then a screened coulomb potential due to a single image charge, as appropriate for the free semiconductor-vacuum interface. Since the proximity of the metal counter-electrode creates multiple image charges whose net effect limits the range of the semiconductor barrier, we may reasonably expect this approximation to provide an upper bound to the image-induced perturbation of the tunneling energy distribution. Employing the well-known expression for the energy-dependent WKB transmission coefficient through a coulomb barrier [32], the relative significance of semiconductor and vacuum terms may be assessed via the dimensionless ratio

$$\left[\beta \left(\frac{1-\beta}{1+\beta} \right) \left(\frac{m^*}{m_0} \right)^{1/2} \right] \left(\frac{\pi}{2} \right) \left(\frac{e^2}{16\pi\epsilon_0\chi s} \right). \quad (32)$$

For typical values of the electron affinity in semiconductors, the last term in parenthesis is of order (1Å/s), while the maximum possible value for the remaining parameters is 0.26. Evaluation for the specific case of Si(111) gives 0.05 (1Å/s) for this ratio. Thus, at gap separations of order ten angstroms or more, the corrections to the maximum of the energy distribution are expected to be small for any material, and certainly negligible for silicon. We can inquire further, under the presumption that the semiconductor barrier will not be negligible under all circumstances, what may at most be expected for the shift in the location of the energy maximum. As an extreme circumstance we retain the screened coulomb potential in the semiconductor, while completely ignoring the vacuum barrier, and find

$$\left(\frac{E_m}{kT} \right)^{3/2} = \left[\beta \left(\frac{1-\beta}{1+\beta} \right) \left(\frac{m^*}{m_0} \right)^{1/2} \right] \left[\left(\frac{\pi}{2} \right) \left(\frac{2m_0}{\hbar^2} \right)^{1/2} \left(\frac{e^2}{16\pi\epsilon_0 kT} \right) \right]. \quad (33)$$

For Si (111) at room temperature, $(E_m/kT) = 0.76$, whereas for optimum parameters it will be no more than a factor of 3 greater.

The above considerations suggest therefore, that, relative to χ , a zero-energy WKB analysis is an appropriate starting point for discussing how image forces influence the apparent barrier height in this system. That supposition is supported by numerical results obtained from the detailed formalism presented in Section II. In particular, Fig. 7 displays the differential current density per unit energy, as a function of gap spacing, calculated for the semiclassical multiple-image interaction using the one electron potential of Fig. 2(a). As one would expect, these distributions show resonant transmission for electron energies very near the conduction band minimum, due to the shallow, long-range attractive portion of the image potential in the semiconductor interior, and, furthermore, they peak just below $(E_z/kT) = 1$, as inferred above. Of particular note in Fig. 7 is that, in marked contrast to the situation for tip induced band bending (Fig. 6), the energy distribution for tunneling electrons appears to be only *weakly dependent* on s (at least when the semiconductor barrier is of finite range), a relevant point outside the scope of our arguments thus far.

As a consequence of the scaling property (5) for the classical image potential in a semiconductor, the zero-energy WKB transmission coefficient through this barrier may be parameterized in terms of the dimensionless integral

$$I(\beta) = \int_{\xi_0(\beta)}^0 [U_s(\beta, \xi)]^{1/2} d\xi . \quad (34)$$

It follows that the contribution of the semiconductor to the apparent barrier height at $E_z = 0$ is given by

$$\frac{\partial \ln D^{\text{semicond}}(E_z = 0, s)}{\partial s} = I(\beta) \left(\frac{m^*}{m_0} \right)^{1/2} \left(\frac{2m_0}{\hbar^2} \right)^{1/2} \left(\frac{e^2}{8\pi\epsilon_0 s} \right)^{1/2} . \quad (35)$$

In relation to the vacuum barrier then, this represents a correction of order

$$\frac{\partial \ln D^{\text{semicond}}(E_z = 0, s) / \partial s}{\partial \ln D^{\text{vac}}(E_z = 0, s) / \partial s} = I(\beta) \left(\frac{m^*}{m_0} \right)^{1/2} \left(\frac{e^2}{32\pi\epsilon_0 \chi s} \right)^{1/2} . \quad (36)$$

Using our estimate above, the last term in parentheses is roughly $(1\text{\AA}/2s)^{1/2}$. Now $I(\beta)$ has a maximum value of 0.51 at $\beta = 1$ (an MVM junction), and decreases smoothly toward zero in the limit that β vanishes. For any reasonable choice of the semiconductor dielectric constant, however, $I(\beta)$ exceeds 0.4. Thus, in general, our correction term can at most be of order $0.3(1\text{\AA}/s)^{1/2}$, and for Si (111) is only a factor of two smaller. Over a physically reasonable range of gap spacings from 10 - 1 \AA , for example, the effect of the semiconductor image potential, in this approximation, will be to *increase* the apparent barrier height between 5 and 15%.

Because of our reliance on a zero-energy analysis, the above estimate presents an upper limit to the magnitude of the effect one may reasonably expect. Indeed, our numerical calculations for Si(111) show that the inclusion of image forces produces a small net *decrease* in the apparent barrier height due to a reduction of the *vacuum* barrier, which is fully consistent with the results for MVM tunneling.

One may pause to consider at this point whether the situation will be fundamentally altered if we replace the far metal electrode with a second semiconductor whose polarizability is less than or equal to that of the first. In this case, the integral (34) diverges (with $|\xi_0| \rightarrow \infty$), since there is no longer any change in sign for $U_S(\beta, \beta', \xi)$ and the image-induced barrier is long range. Reflecting on (33), however, we are reminded that this barrier will be probed not at $E_z = 0$, but rather at $E_z = kT$. The effective range of the image interaction at this energy is then of order

$$z_{kT} = \beta \left(\frac{1-\beta}{1+\beta} \right) \left(\frac{e^2}{16\pi\epsilon_0 kT} \right), \quad (37)$$

which, at $T = 300$ K, is less than 25 \AA for optimum β . Thus, there is nothing in our arguments which leads us to suspect circumstances will be dramatically different for semiconductor-vacuum-semiconductor (SVS) tunneling, unless one can arrange to conduct the experiments at low temperature.

V. Summary and Conclusions

We have investigated the influence of the image potential on tunneling through a planar metal-vacuum-semiconductor junction. This problem differs qualitatively from the metal-vacuum-metal junction because there is now an image potential in the semiconductor interior as well as in the vacuum region. The classical multiple-image expression for an MVS system has been extended,

using a Thomas-Fermi like dielectric function in the semiconductor together with the usual Thomas-Fermi theory for the metal, to provide expressions which are everywhere finite. The resulting semiclassical image potentials in semiconductor, vacuum, and metal must still be smoothly joined, however, by an interpolation through the interfaces. Using these potentials, the tunneling current at finite temperature was calculated as a function of separation for the particular case of a *n*-type hydrogen-passivated Si(111) - Au system, and an apparent barrier height Φ_A then extracted to simulate the results of STM modulation experiments.

To obtain a more general understanding of these detailed calculations, qualitative arguments based on a WKB picture have also been presented. If the image potential is neglected, Φ_A is well described by terms involving, first, the semiconductor's electron affinity, and, second, the effect of tip-induced band bending. When the contribution of the image potential within the semiconductor is separately considered, a WKB estimate indicates it will perturb the apparent barrier height by at most 10% at reasonable tip-sample distances. This crude estimate helps one understand the principal result of the detailed calculations presented in Figures 3 and 4: Although the tunneling barrier for an MVS junction differs from that for an MVM junction, the image potential in the semiconductor makes only a modest contribution to the apparent barrier height. Furthermore, as our calculations reveal, the dominant effect is a slight lowering of Φ_A , due to the attractive image potential in the vacuum region in conformity with expectations based on MVM tunneling, rather than any increase in Φ_A from the repulsive image potential within the semiconductor.

One may have thought that the semiconductor's internal image potential, being long-range, would have a substantial effect on carriers originating from the bulk conduction band edge, and thus influence not only tunneling currents, but the apparent barrier height as well. Our calculations, together with the WKB analysis, indicate otherwise. Three qualitative arguments account for this observation: First, in the case of flat bands, the potential due to polarization charge at the vacuum-metal interface competes with that of the semiconductor-vacuum interface to produce a barrier in the semiconductor interior which is short range; Second, for the more general case which includes a semiconductor diffusion potential in either depletion or weak inversion, the overwhelming influence on the carrier distribution arises from the diffusion potential, and not the image potential. In the case this diffusion potential is tip-induced, we have shown explicitly that Φ_A is almost completely dominated by the distance dependence of field penetration in the semiconductor, and that image effects are of relatively minor importance; Finally, for flat band conditions, most of the tunneling current is provided by electrons whose energy is of order kT above the band edge. For these electrons, the image-induced barrier is effectively short range at room temperature, even if

one neglects the influence of polarization charge at the metal tip. The same argument applies, in principle, to the semiconductor-vacuum-semiconductor junction, but whether or not the image potential will have a significant influence in this system at low temperatures remains an open question.

Acknowledgements

We gratefully acknowledge J. A. Kramar for providing part of the computer codes on which these calculations were based. This work was supported by the Office of Naval Research under Grant Nos. N00014-89-J-3029 and N00014-91-J-1126, and by the Robert A. Welch Foundation.

References

1. J.G. Simmons, *J. Appl. Phys.* **34**, 2581 (1963).
2. J.G. Simmons, in *Tunneling Phenomena in Solids*, E. Burstein and S. Lundqvist, Eds. (Plenum, New York, 1969).
3. N.M. Miskovsky, P.H. Cutler, T.E. Feuchtwang, and A.A. Lucas, *Applied Phys. A* **27**, 139 (1982).
4. N.D. Lang and W. Kohn, *Phys. Rev. B* **7**, 3541 (1973).
5. N.D. Lang, *Solid State Physics* **28**, 225 (1973).
6. G. Binnig, N. Garcia, H. Rohrer, J.M. Soler, and F. Flores, *Phys. Rev. B* **30**, 4816 (1984).
7. N.D. Lang, *Phys. Rev. B* **37**, 10395 (1988).
8. J.H. Coombs, M.E. Welland, and J.B. Pethica, *Surf. Sci.* **198**, L353 (1988).
9. J. Bono and R.H. Good, *Surf. Sci.* **151**, 543 (1985).
10. J. Mahanty and M.T. Michalewicz, *J. Phys. C* **19**, 5005 (1986).
11. H. Morawitz, I.P. Batra, R. Reinisch, and G.R. Henry, *Surf. Sci.* **180**, 333 (1987).
12. A.A. Lucas, et al., *Phys. Rev. B* **37**, 10708 (1988).
13. S. Ossicini and M. Bertoni, *Phys. Rev. B* **35**, 848 (1987).
14. R. Garcia, *Phys. Rev. B* **42**, 5476 (1990).
15. B.N.J. Persson and A. Baratoff, *Phys. Rev. B* **38**, 9616 (1988).
16. J. Bono and R.H. Good, *Surf. Sci.* **175**, 415 (1986).
17. M. Kleefstra and G.C. Herman, *J. Appl. Phys.* **51**, 4923 (1980).
18. A. Tugulea and D. Dascalu, *J. Appl. Phys.* **56**, 2823 (1984).
19. R. Browning, M.A. Sobolewski, and C.R. Helms, *Phys. Rev. B* **38**, 13407 (1988).
20. J.C. Inkson, *J. Phys. C* **6**, 1350 (1973).
21. Z.-H. Huang, M. Weimer, and R.E. Allen, *J. Vac. Sci. Technol. B* **9**, 2399 (1991).

22. M. Weimer, J. Kramar, and J.D. Baldeschwieler, *Phys. Rev. B* **39**, 5572 (1989).
23. J.C. Inkson, *J. Phys. C* **4**, 591 (1971).
24. D.M. Newns, *J. Chem. Phys.* **50**, 4572 (1969).
25. N.W. Ashcroft and N.D. Mermin, *Solid State Physics* (Holt, New York, 1976).
26. J.P. Walter and M.L. Cohen, *Phys. Rev. B* **2**, 1821 (1970).
27. S.M. Sze, *Physics of Semiconductor Devices* (Wiley, New York, 1981).
28. J.A. Kramar, Ph. D. Thesis, California Institute of Technology (1990).
29. E.H. Rhoderick and R.H. Williams, *Metal-Semiconductor Contacts, Second edition* (Oxford University Press, New York, 1988).
30. F.A. Padovani and R. Stratton, *Solid-St. Electron.* **9**, 695 (1966).
31. C.R. Crowell and V.L. Rideout, *Solid-St. Electron.* **12**, 89 (1969).
32. L.D. Landau and E.M. Lifshitz, *Quantum Mechanics (Non-relativistic Theory), Third edition* (Pergamon, 1977).

Figure Captions

- Figure 1: (a) Schematic energy diagram for an ideal semiconductor-vacuum-metal junction at zero applied bias V , neglecting image effects. Φ is the metal work function, E_F the metal Fermi energy, χ the semiconductor electron affinity, and ϕ_n the offset from the Fermi level to the bottom of the semiconductor conduction band. The drawing is not to scale since the depletion width W is typically much greater than the gap spacing s , and χ exceeds the band gap, $E_c - E_v$.
- (b) Flat band situation when the applied bias V_{FB} has been chosen to eliminate the electric field arising from a difference in metal and semiconductor work functions, $\Phi - (\chi + \phi_n)$.
- Figure 2: (a) Effective one-electron potential energy as a function of position for $V = V_{FB}$ and $s = 10 \text{ \AA}$. Solid line: including the semiclassical image potential with interpolation. Dotted line: including the classical image interaction. Dashed line: neglecting image effects. $\chi = 4.3 \text{ eV}$, $\Phi = 5.1 \text{ eV}$, and $E_F = 5.53 \text{ eV}$. The potentials are independent of doping.
- (b) Effective one-electron potential energy as a function of position at a representative bias which produces depletion in the semiconductor ($N_d = 5 \times 10^{17} \text{ cm}^{-3}$). All other parameters as above. Solid line: including the semiclassical image potential with interpolation. Dashed line: neglecting image effects. Note the offset of the semiconductor surface potential from the conduction band edge in the bulk.
- Figure 3: Tunneling current density j versus electrode separation s as a function of doping for fixed bias and $T = 300 \text{ K}$. Solid line: including the semiclassical image potential as in Figure 2(b). Dashed line: neglecting image effects.
- Figure 4: Apparent barrier height Φ_A versus electrode separation s as a function of doping. Solid line: including the semiclassical image potential. Dashed line: neglecting image effects. The flat band results are essentially independent of doping in the non-degenerate regime.
- Figure 5: Tunneling current density j versus applied bias V as a function of doping for fixed separation and $T = 300 \text{ K}$. Solid line: including the semiclassical image potential. Dashed line: neglecting image effects. The current density and applied bias are scaled to their respective flat band values to facilitate a comparison of the shape of the $j - V$ characteristics.
- Figure 6: Differential tunneling current density distribution versus normal energy E_z (scaled to the semiconductor surface potential) as a function of electrode separation, neglecting image effects, for $V = -100 \text{ mV}$ and $N_d = 5 \times 10^{17} \text{ cm}^{-3}$. Inset: tip-induced semiconductor surface potential versus separation at the same fixed bias.
- Figure 7: Differential tunneling current density distribution versus normal energy E_z (scaled to kT) as a function of electrode separation, including the semiclassical image potential in the absence of tip-induced band bending ($V = V_{FB}$).

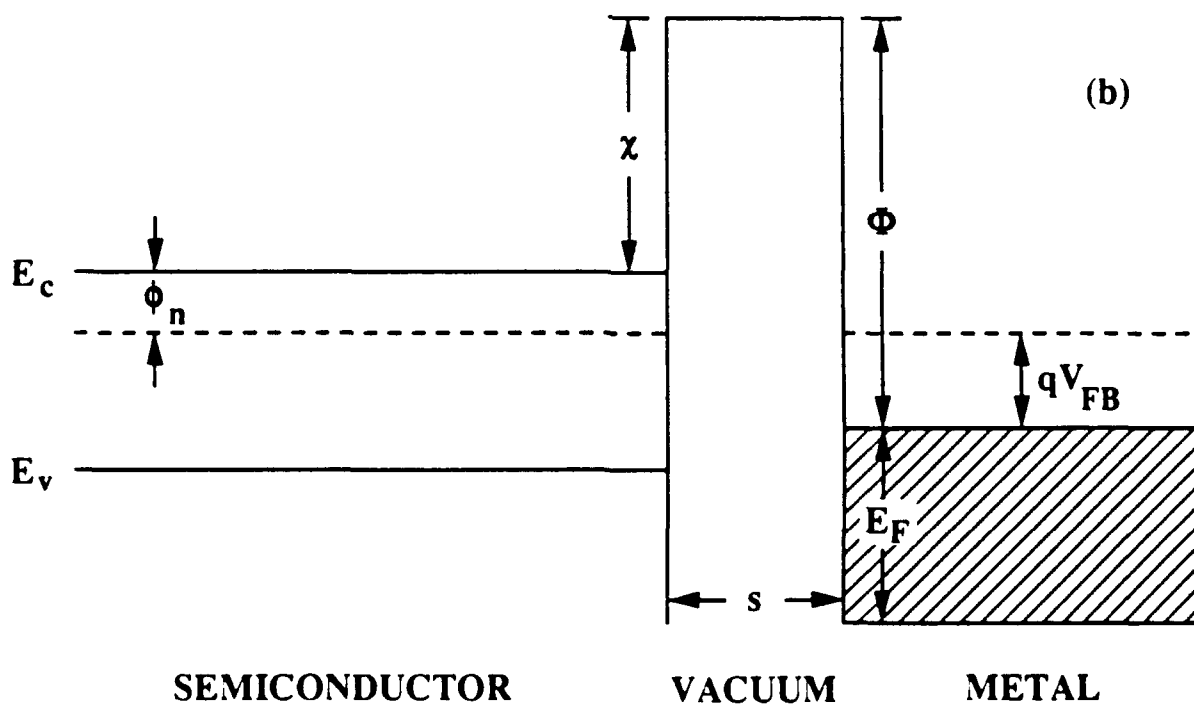
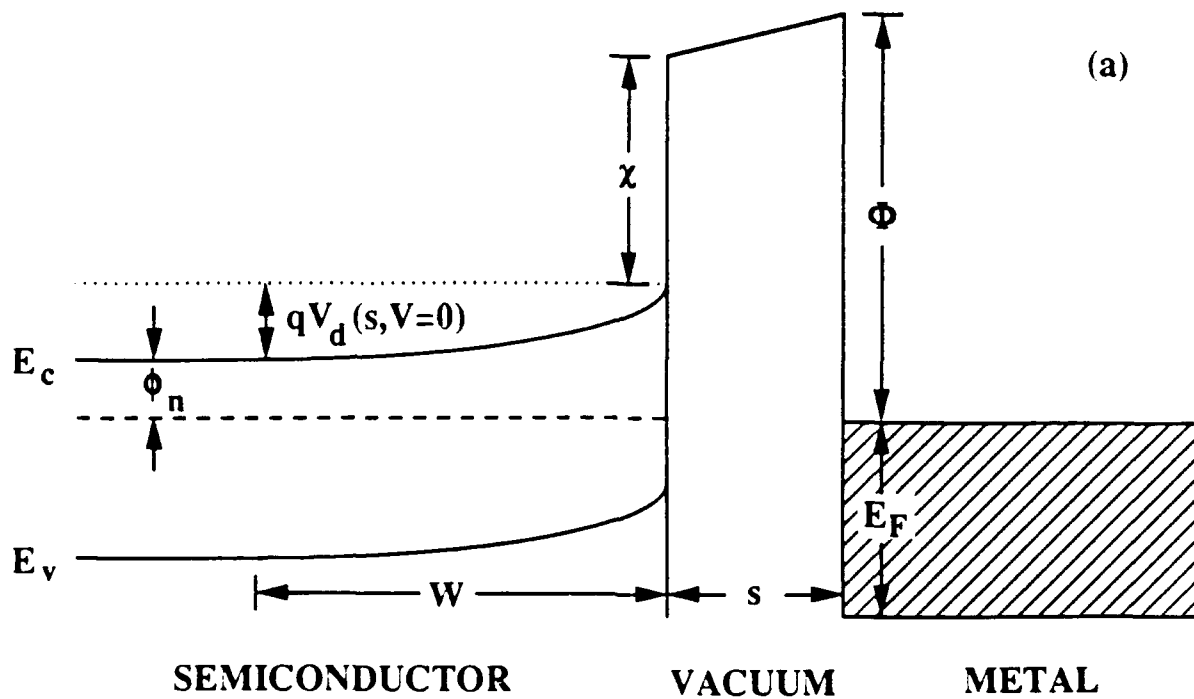


Figure 1

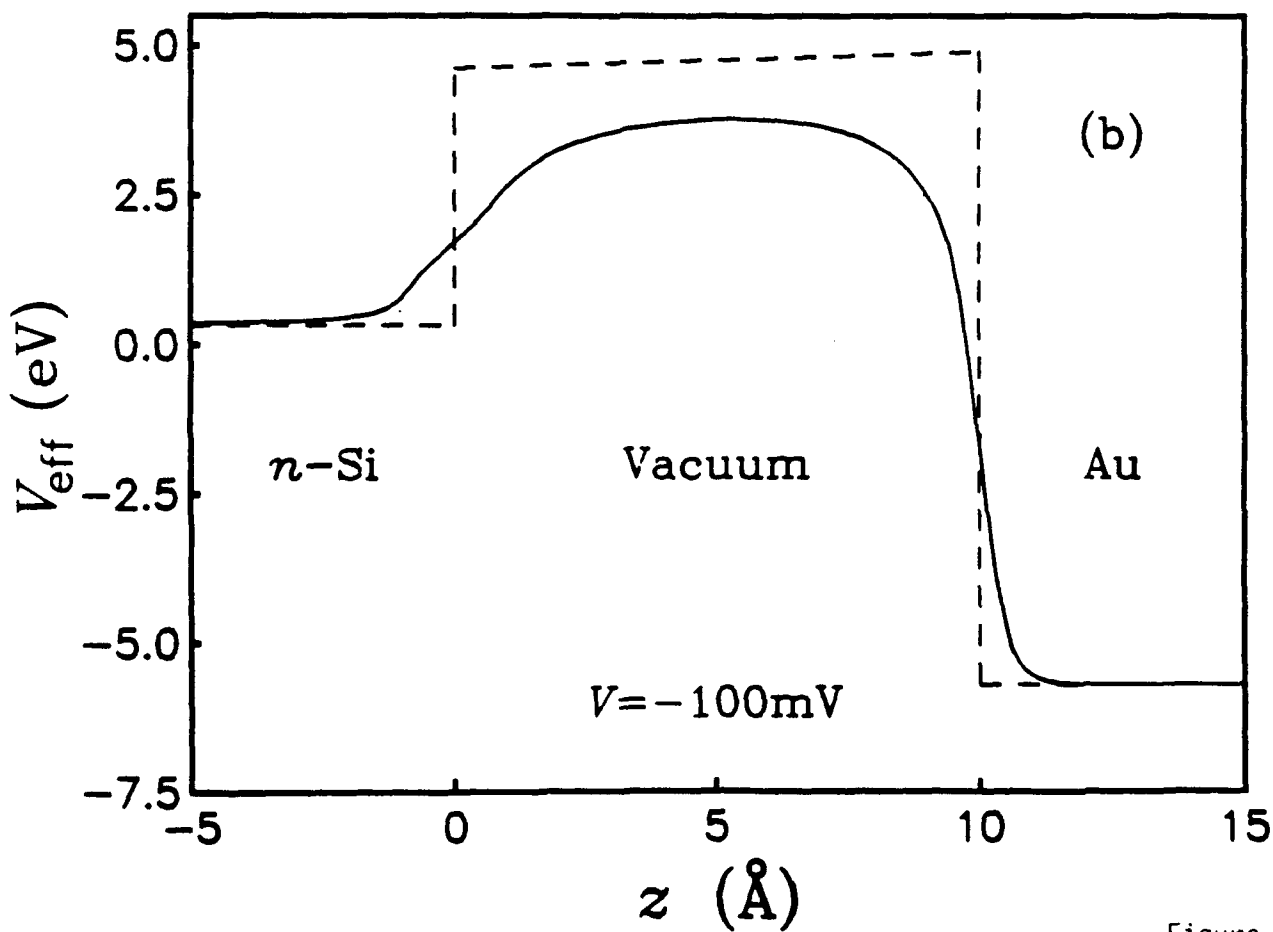
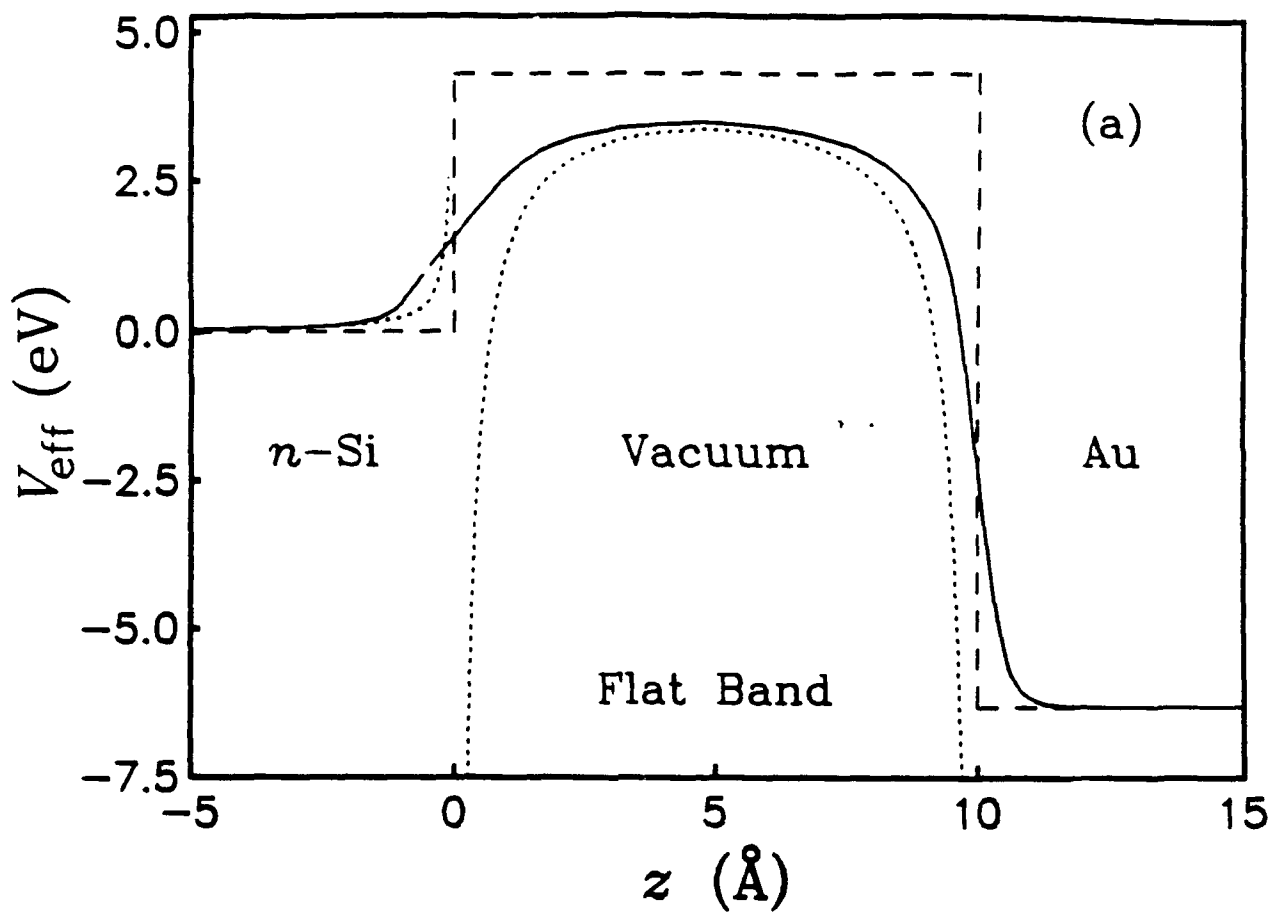


Figure 2

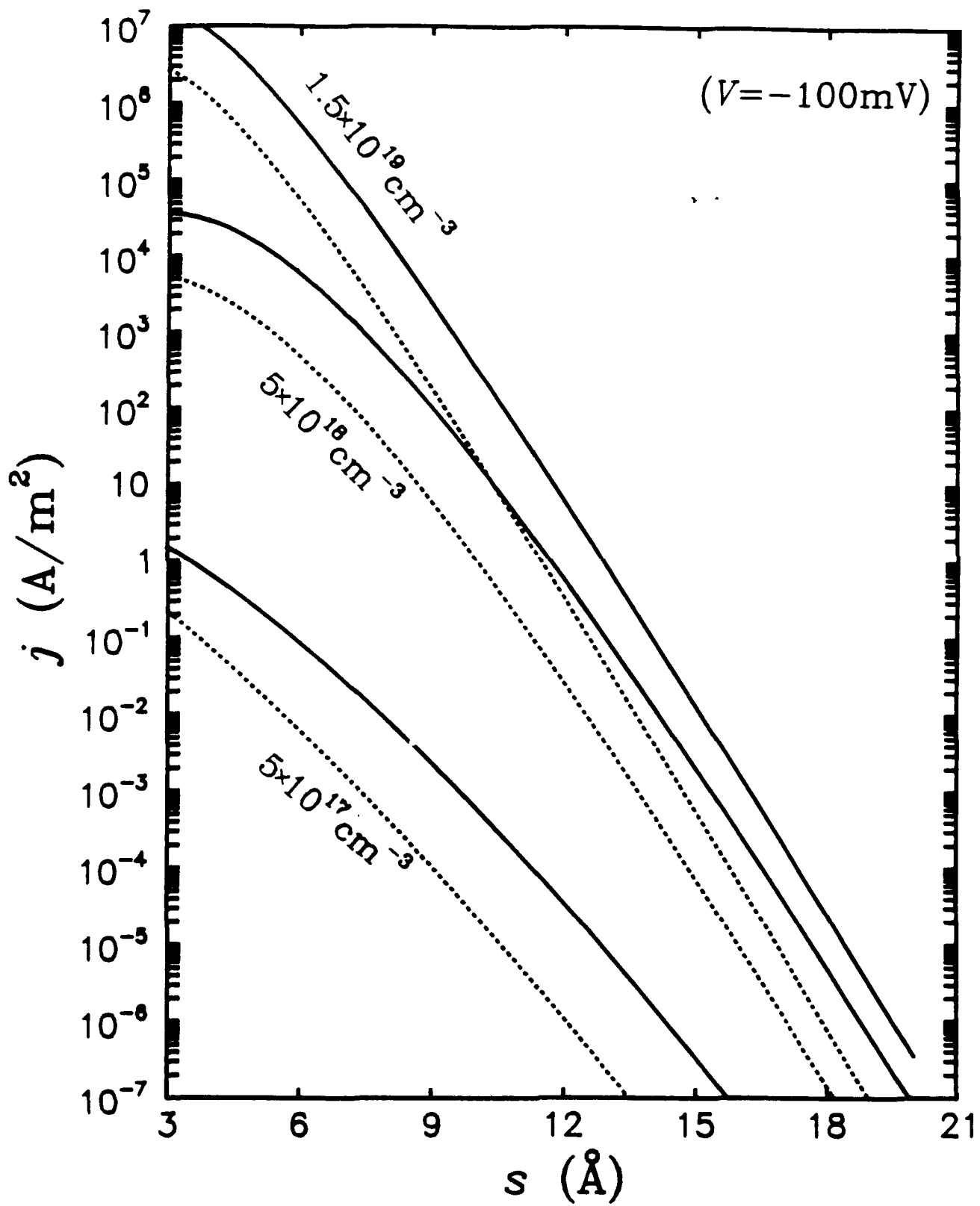


Figure 3

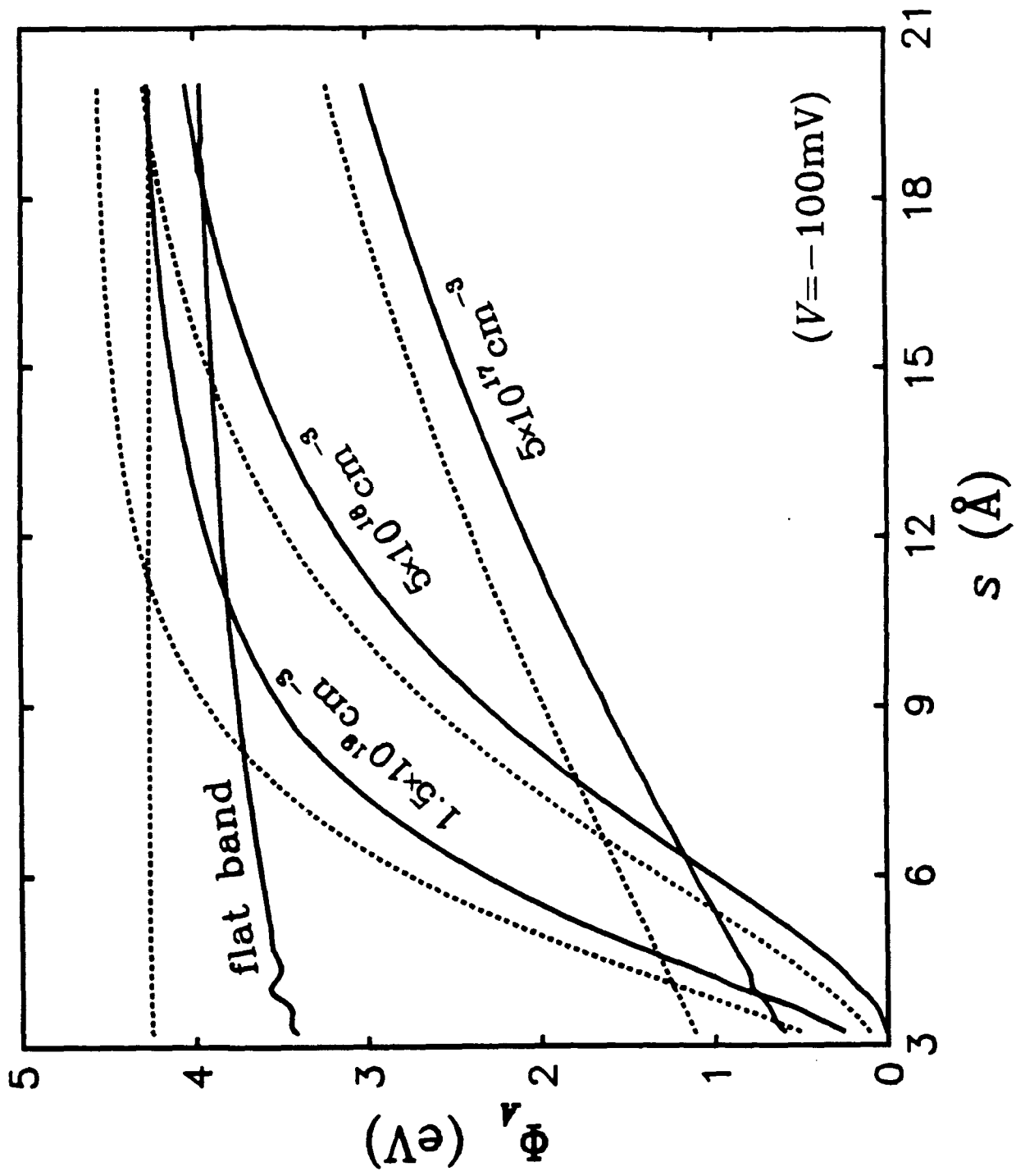


Figure 4

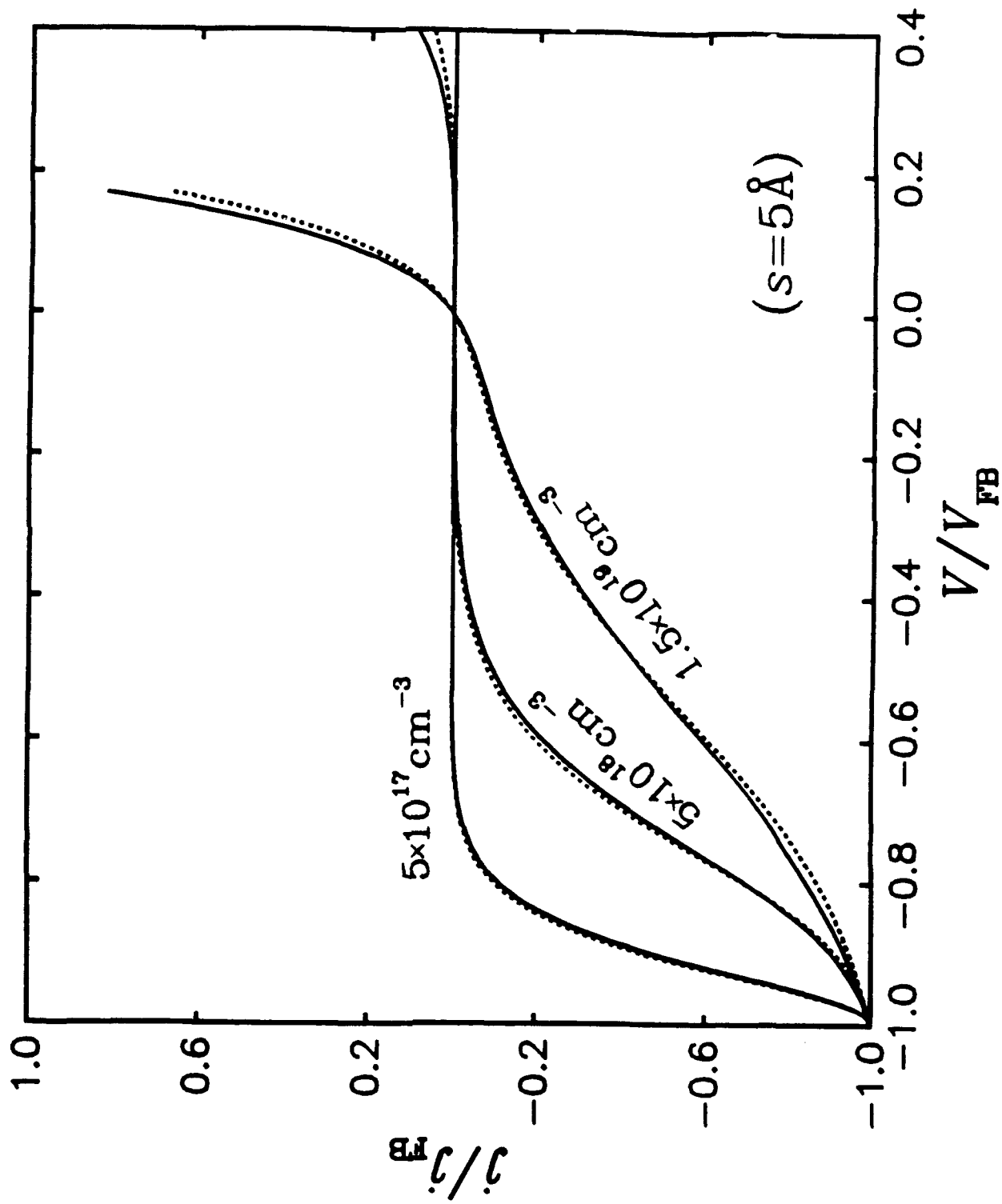


Figure 5

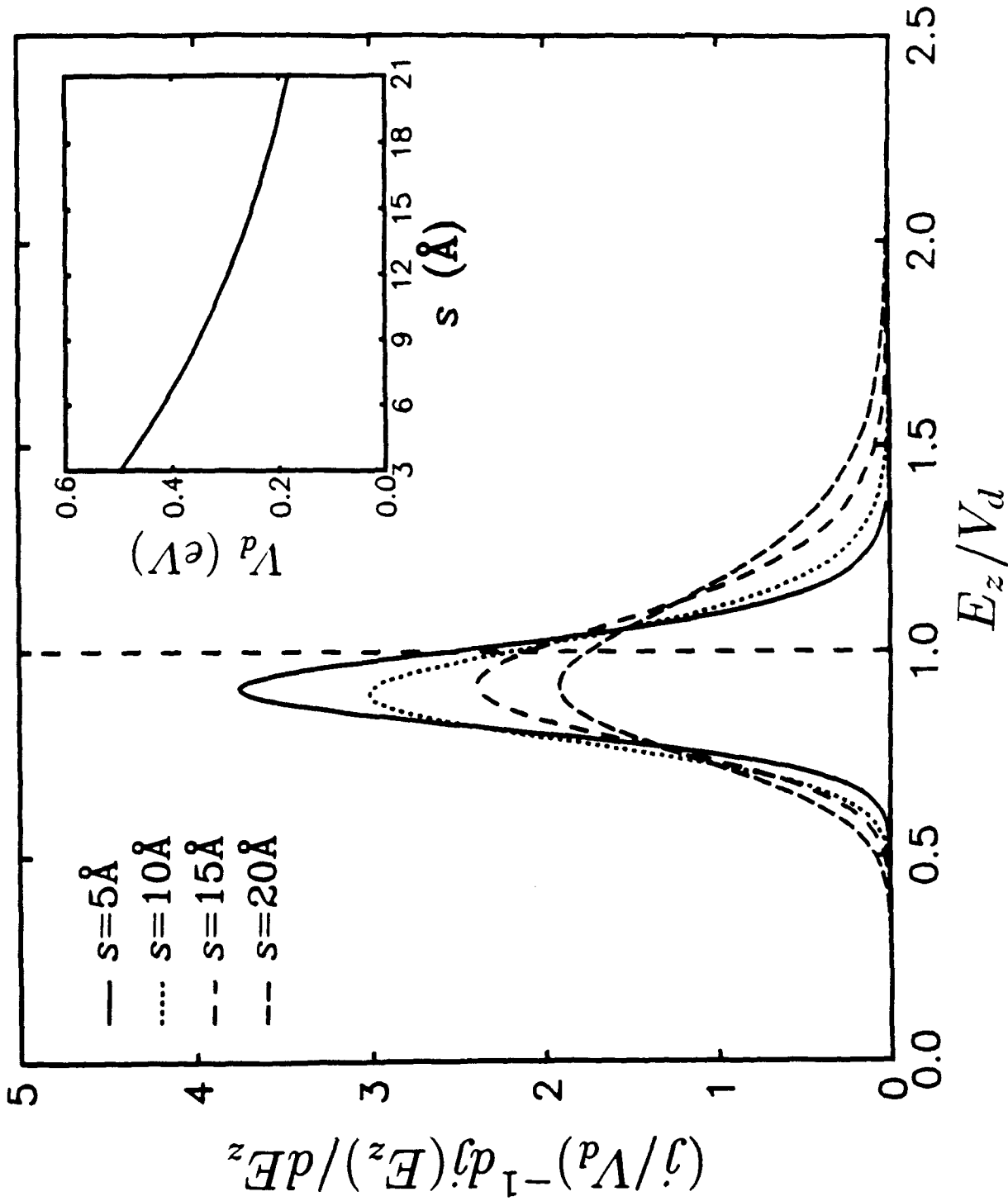


Figure 6

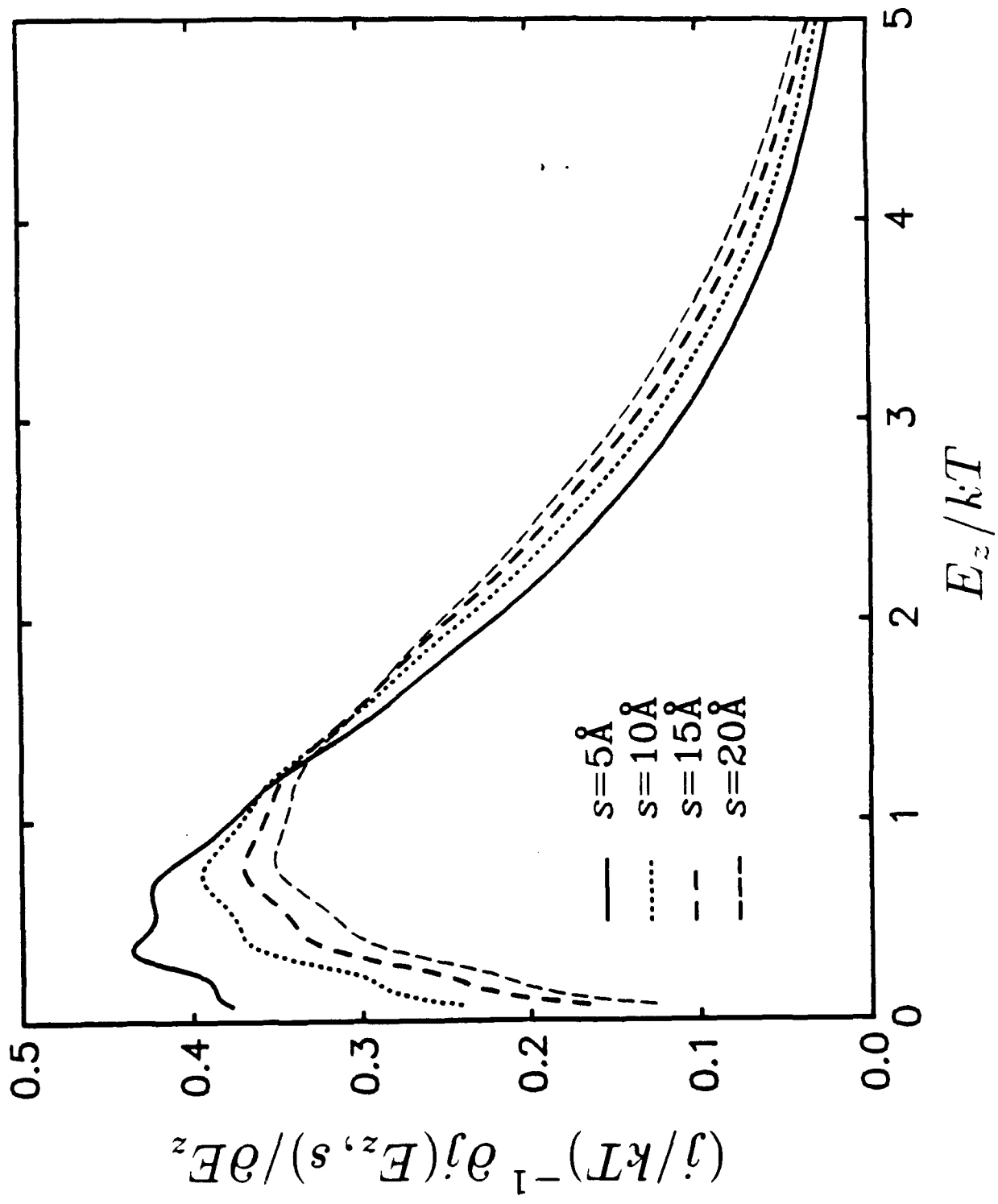


Figure 7

Section II

INSTRUMENTATION

Figure Captions

Figure 1(a-b): UHV STM system in Surface Physics Laboratory at Texas A&M University. The entire assembly rests atop a specially engineered vibration isolation platform.

Figure 2(a): Orthographic views of main analytical chamber. Flanges are arranged along the chamber axis in three clusters. From left to right: Surface analytical cluster with provision for Auger Spectroscopy, LEED, X-ray Photoelectron Spectroscopy, and Ion Sputtering; Sample pick-off from preparation chamber / entry lock with provision for sample storage; STM cluster. Maximum flexibility is maintained by the orthogonal arrangement of 8" ports in the STM cluster, permitting bottom, top, or side mounting of an STM flange. Introduction of samples to the main chamber and movement along the axis of this chamber is via orthogonal, magnetically coupled linear/rotary transporters.

Figure 2(b): Schedule describing location, orientation, and function of various ports available on the analytical chamber, as well as sample target positions.

Figure 3(a): Orthographic views of UHV pumping assembly consisting of Perkin-Elmer 220 L/sec D-I ion pump, titanium sublimation pump with liquid nitrogen cooled cryoshroud, and custom mounting for SAES nonevaporable getter (NEG) module. Auxiliary flanges for ion gauge and/or quadrupole mass spectrometer.

Figure 3(b): Small volume sample preparation chamber for directed gas-phase dosing, electrochemical deposition cells, or filament evaporators. A gate valve separating this side chamber from the main analytical volume permits dosing with high vapor pressure substances without the risk of either contaminating analytical instruments or exposing the STM tip. A 30 L/sec Perkin-Elmer D-I ion pump and Balzer's 60 L/sec turbo-molecular pump, attached to the entry lock, provide pumping for this isolated segment.

Figure 4(a): Ambient (vertical) vibration amplitude versus frequency, on laboratory floor (upper trace) and atop vibration isolation platform (lower trace). Vertical scale: logarithmic, from -60 db (= 1 pm) to +40 db (= 100 nm), with 10 db per division. Dashed line indicates 0 db (= 1 nm) displacement. Horizontal scale: linear, from 0 Hz to 50 Hz, with 5 Hz per division and a frequency resolution of 0.125 Hz. Platform resonance occurs at 1.25 Hz and unity gain crossover in the transfer function occurs at 1.625 Hz. The 1 nm displacement crossover frequency is 4.00 Hz. Above 1.625 Hz, the platform successfully filters out vertical seismic disturbances, reaching an ultimate suppression factor greater than 40 db beyond 10 Hz.

Figure 4(b): Ambient (horizontal) vibration amplitude versus frequency, on laboratory floor (upper trace) and atop vibration isolation platform (lower trace). Vertical and horizontal scales as in 4(a). Platform resonance occurs at 1.125 Hz and unity gain crossover in the transfer function occurs at 1.50 Hz. The 1 nm displacement crossover frequency is 3.00 Hz in this case. Ultimate suppression above 10 Hz is between 30 db and 40 db, depending on frequency.

Figure 5(a): Finite-element simulation (ALGOR) of normal modes for magnetically coupled linear/rotary transporters fixed at one end (cantilevered support). Lowest vibrational resonance occurs at approximately 25 Hz.

Figure 5(b): Finite-element simulation of normal modes for magnetically coupled linear/rotary transporters fixed at both ends. Lowest vibrational resonance has been shifted to approximately 87 Hz.

Figure Captions (cont'd)

Figure 6(a-b): Normal modes of center- and transverse-axis magnetically coupled linear/rotary transporters in rigidized support scheme implemented in Figure 1. Note that lowest resonant frequency is close to that of ideal fixed-fixed boundary conditions in Figure 5(b) above.

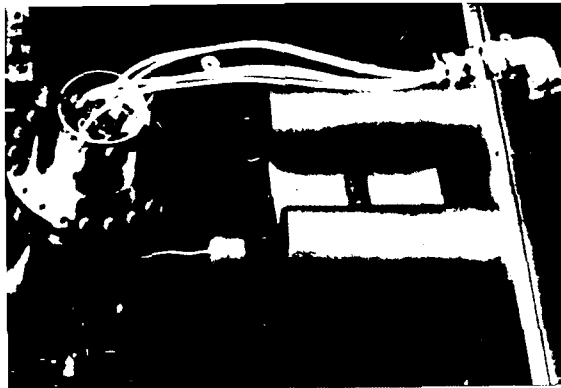
Figure 7(a-b): Close-up view of Omicron STM which shows flange mounting, single-stage spring suspension with eddy-current damping, coarse two-dimensional sample positioner (left center), piezo-tripod with exchangeable tip holder (right center), and BEEM current preamplifier (bottom center). Hidden from view by supports for spring suspension is tunneling current preamplifier mounted directly behind the piezo scanner.

Figure 8: View along main axis of analytical chamber, through port 1: Looking past Cylindrical Mirror Analyzer (in foreground), infra-red bake out lamps, and sample carousel, toward STM (in background) with stage at transfer elevation, and pincer-grip wobble stick. Center-axis transporter, holding tip or sample, is positioned just above STM.

Figure 9(a-b): Cross-section through main chamber at ports 6,7,8 and 9, illustrating proposed pick-off scheme after sample introduction from entry lock or preparation chamber. Wobble stick, sample plattens, and carousel are Omicron design. Wobble stick includes pincer movement for positive grip on platten. Sample plattens are shown mounted on custom rack attached to the end of a magnetic linear/rotary transporter with 30" stroke. Overhead view port allows convenient inspection of transfer process and loaded carousel. Wobble stick retraction is sufficient for plattens to be exchanged from front to back on carousel, thereby permitting a reversal of their orientation relative to chamber center line once the carousel is rotated. This is crucial as sample and tip loading must proceed with opposite orientation in the STM. Rotation of carousel is accomplished by tapping a clutch lever, which is inside a 20 degree cone angle, with wobble stick. A high conductance, stainless steel mesh screen serves to protect the pumping assembly from any inadvertently dropped plattens.

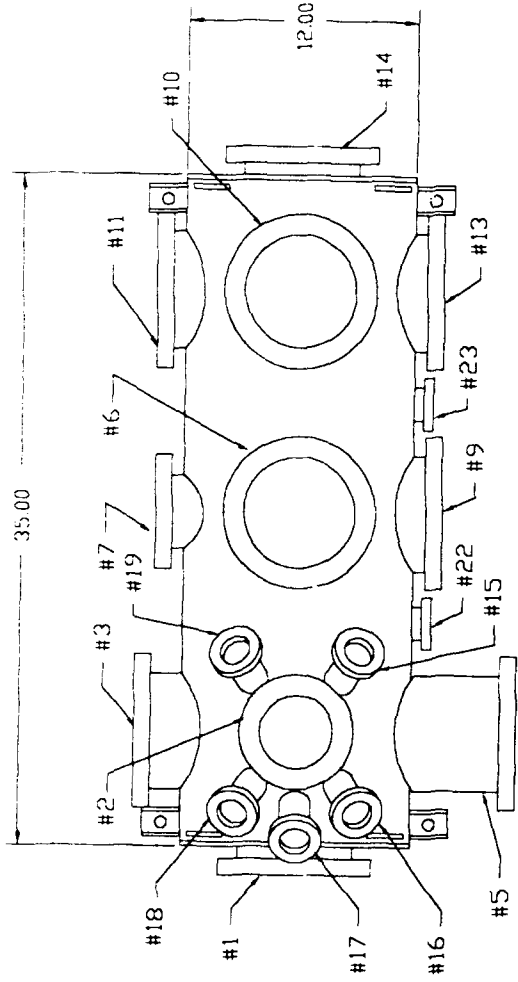
Figure 10(a): Cross-section through main chamber at ports 10,11,12 and 13, showing relative orientation of center-line magnetic linear/rotary transporter and a second pincer-grip wobble stick during the initial stage of sample or tip transfer to STM. Overhead and side view ports facilitate inspection of transfer process.

Figure 10(b): Once magnetic transporter has been fully withdrawn, sample or tip may be loaded onto the STM stage by levelling wobble stick as shown.

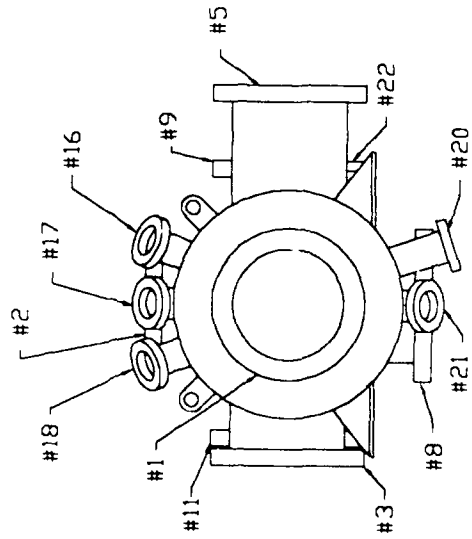




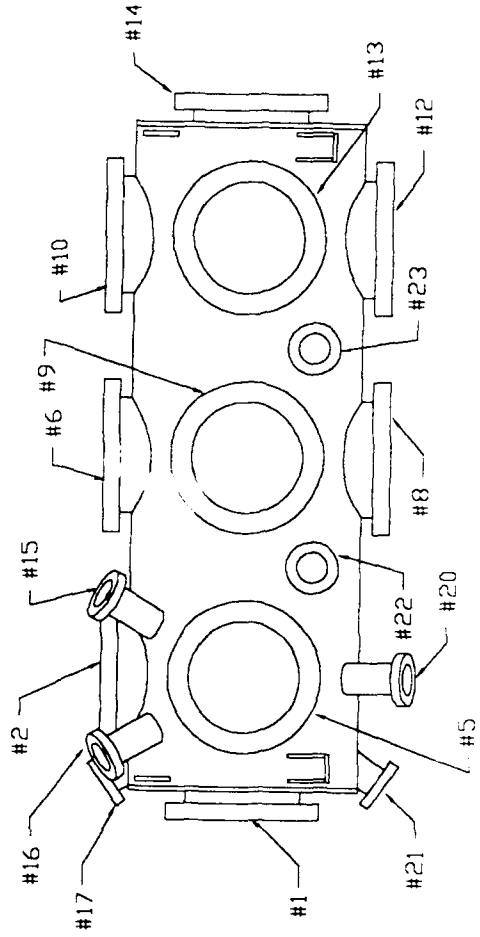
SCALE: 1" = 10"



TOP VIEW

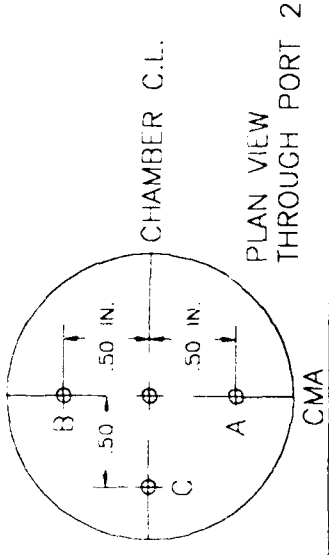


SIDE VIEW

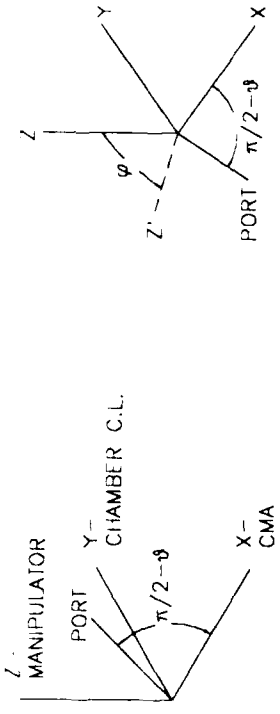


FRONT VIEW

Figure 2(a)



PLAN VIEW THROUGH PORT 2
THROUGH PORT 2

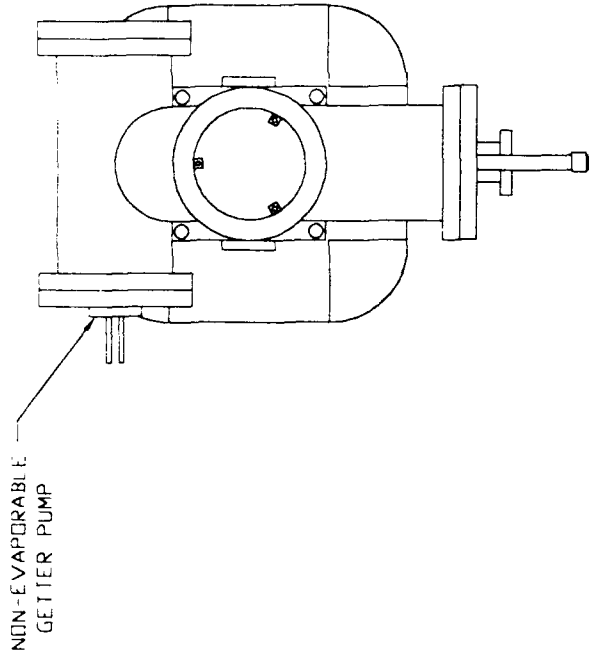


PORTS	FLANGE			TUBULATION			TARGET			ALIGNMENT TOLERANCES	
	PURPOSE	NOMINAL O.D.	I.D.	SUPPLIED VIEWPORT/BLANKOFF	O.D.	WALL THICKNESS	TARGET POINT	FLANGE TO TARGET DISTANCE	θ (DEG)		φ (DEG)
1	SCA	8.00	5.84	V	6.00	.08	C	7.00 ^{+0.00} _{-.06}	--	--	.020"R
2	MANIPULATOR	6.00	3.84	--	4.00	.08	φ	7.50 ± 0.3	--	--	.020"R
3	RV LEED	8.00	5.84	B	6.00	.08	B	8.00 ^{+0.00} _{-.06}	--	--	.020"R
4	--	--	--	--	--	--	--	--	--	--	--
5	CMA	8.00	5.84	--	6.00	.08	A	11.00 ^{+0.00} _{-.06}	--	--	.020"R
6	VIEWPORT	8.00	5.84	V	6.00	.08	C.L.	7.50 ± 0.6	--	--	--
7	ENTRY LOCK / PREP CHAMBER	6.00	3.84	--	4.00	.08	C.L.	7.50 ± 0.6	--	--	.020"R
8	PUMPING	8.00	5.84	--	6.00	.08	C.L.	7.50 ± 0.6	--	--	--
9	SAMPLE PICKOFF	8.00	5.84	B	6.00	.08	C.L.	7.50 ± 0.6	--	--	--
10	VIEWPORT	8.00	5.84	V	6.00	.08	C.L.	7.50 ± 0.3	--	--	--
11	--	8.00	5.84	B	6.00	.08	C.L.	7.50 ± 0.3	--	--	--
12	STM	8.00	5.84	B	6.00	.08	C.L.	7.50 ± 0.3	--	--	--
13	--	8.00	5.84	B	6.00	.08	C.L.	7.50 ± 0.3	--	--	--
14	MAGNETIC TRANSPORT	8.00	5.84	B	6.00	.08	φ	7.50 ± 0.6	--	--	.060"R
15	--	2.75	1.63	B	1.75	.06	A	9.00 ± 0.3	18.0	-30.0	.020"R
16	--	2.75	1.63	B	1.75	.06	A	9.00 ± 0.3	18.0	30.0	.020"R
17	X-RAY SOURCE	2.75	1.63	B	1.75	.06	C	9.00 ± 0.3	0.0	35.3	.020"R
18	--	2.75	1.63	B	1.75	.06	B	9.00 ± 0.3	-18.0	30.0	.020"R
19	--	2.75	1.63	B	1.75	.06	B	9.00 ± 0.3	-18.0	-30.0	.020"R
20	SPUTTER GUN	2.75	1.63	B	1.75	.06	A	9.00 ± 0.3	18.0	180.0	.020"R
21	X-RAY SOURCE	2.75	1.63	B	1.75	.06	C	9.00 ± 0.3	0.0	144.7	.020"R
22	IR LAMP	2.75	1.63	B	1.75	.06	--	--	--	--	--
23	IR LAMP	2.75	1.63	B	1.75	.06	--	--	--	--	--

CHAMBER		ENDCAPS		MATERIAL	
O.D.	WALL THICKNESS	O.D.	THICKNESS	CHAMBER & PORT TUBULATION - 304 SS	
12.00	.125	12.00	.250	ALL FLANGES NON-ROTATABLE	

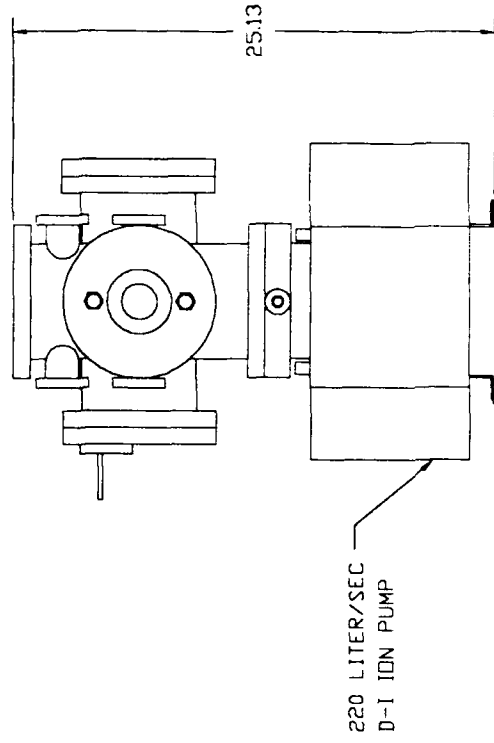
Figure 2(b)

TOP VIEW



SCALE: 1" = 10"

FRONT VIEW



SIDE VIEW

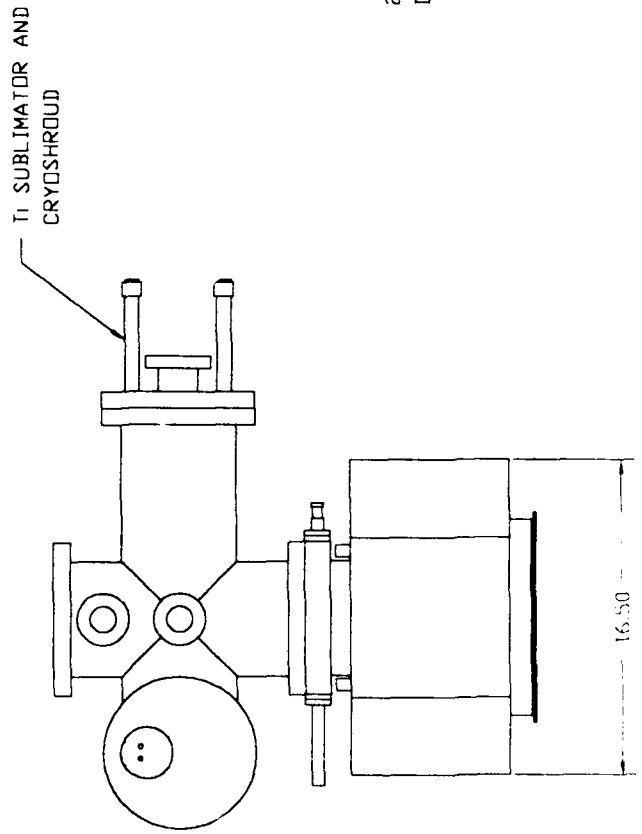
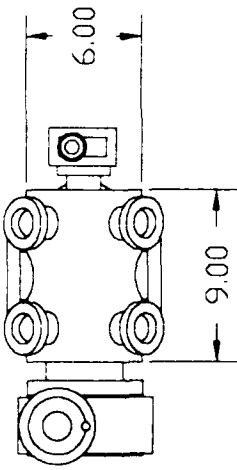


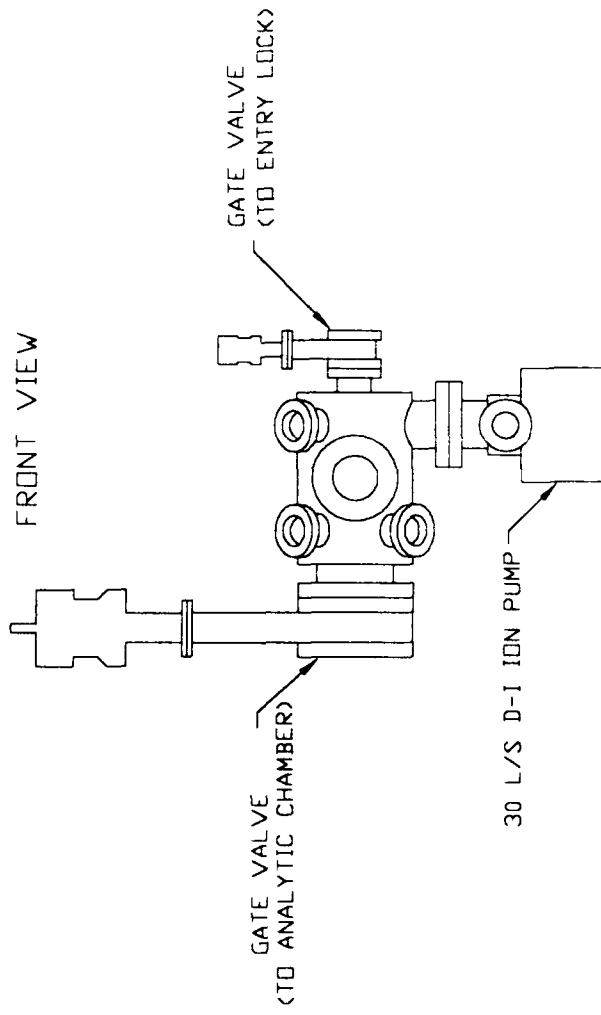
Figure 3(a)

SCALE: 1" = 10"

TOP VIEW



FRONT VIEW



SIDE VIEW

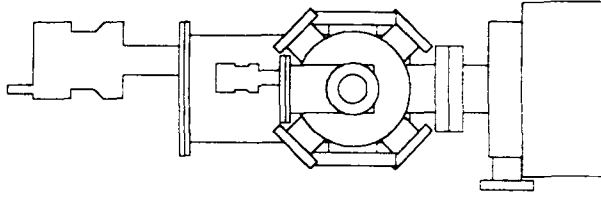


Figure 3(b)

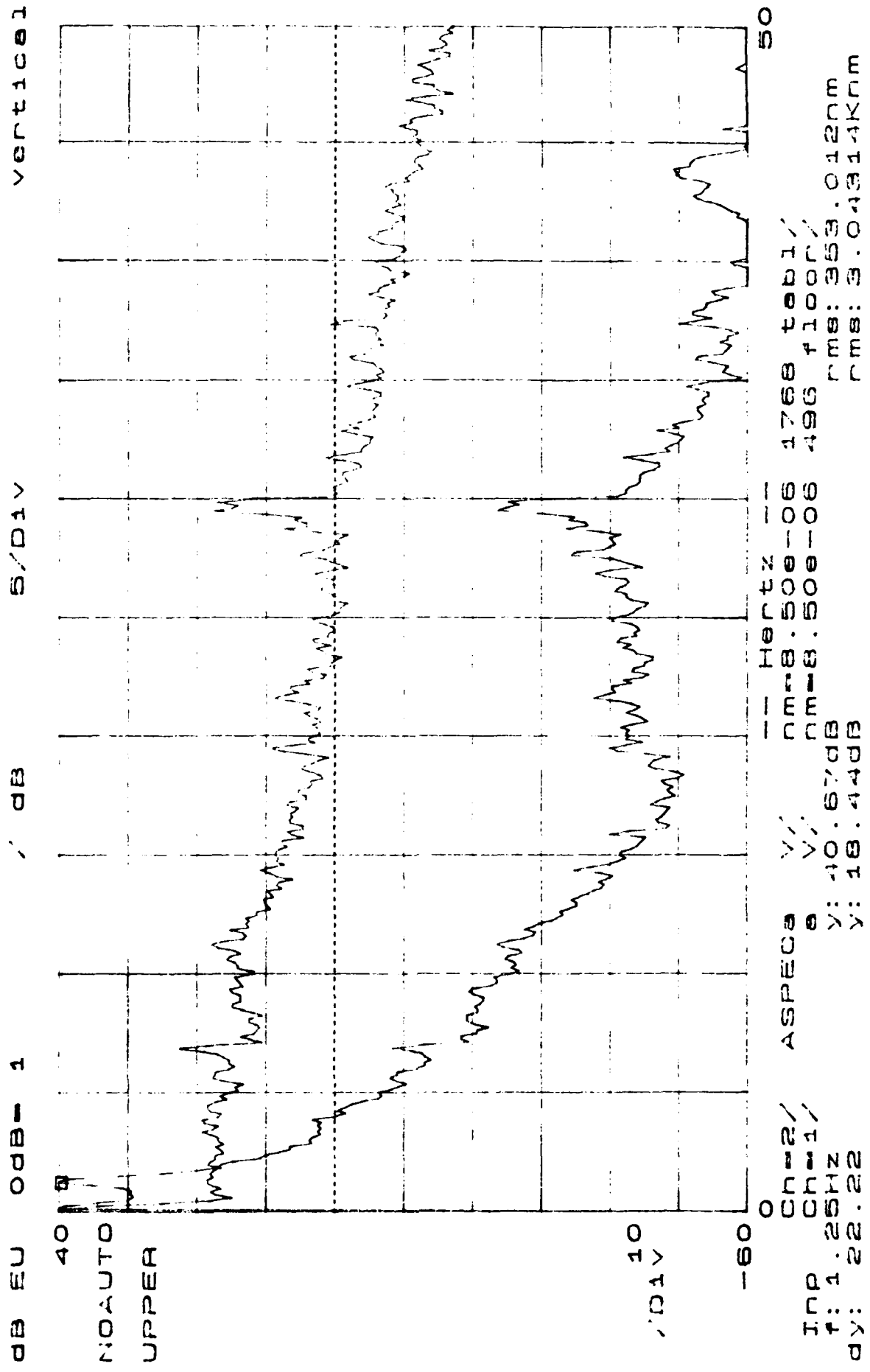
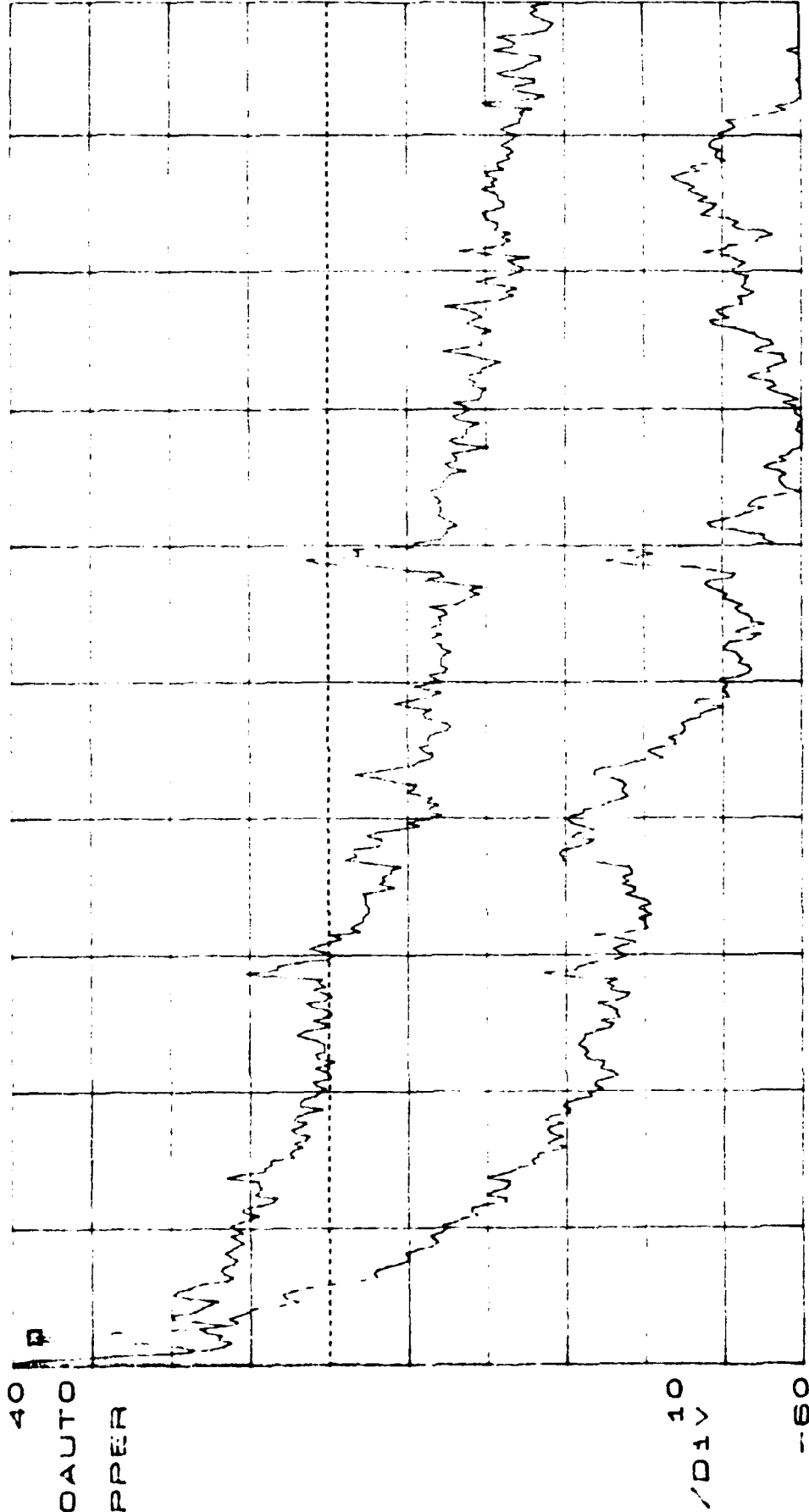


Figure 4(a)

dB EU 0dB= 1 / dB 5/DIV Horizontal

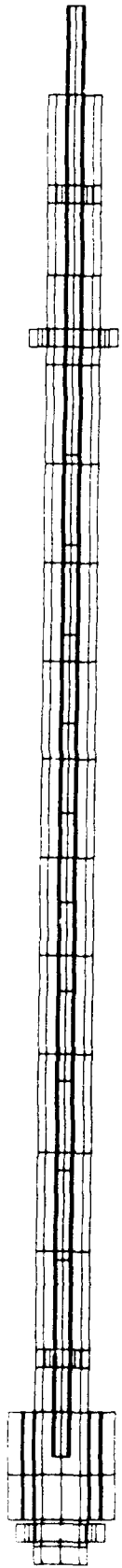


CH=2/ ASPECA V// nm=8.50e-06 1768 tab1/
 CH=1/ ASPECA V// nm=8.50e-06 1768 tab1/
 f: 1.125Hz y: 37.03dB rms: 8.86594Knm
 dy: 23.51 y: 13.52dB rms: 6.98768Knm

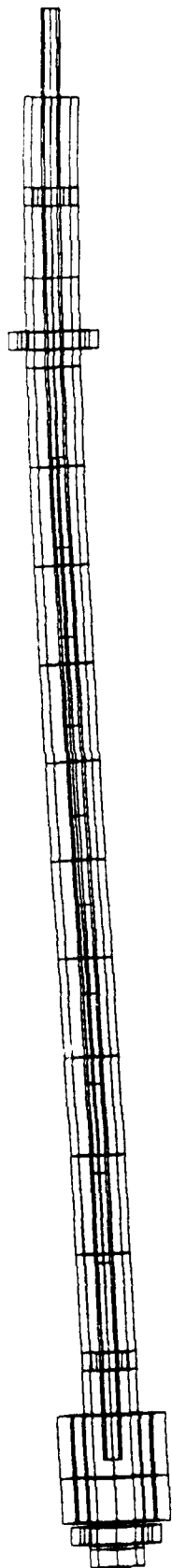
Date taken MON. 5/28/90 9:34 AM

Wed JUL 11 13:42:36 1990

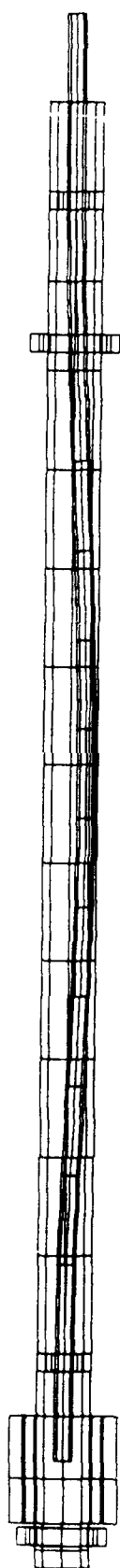
Figure 4(b)



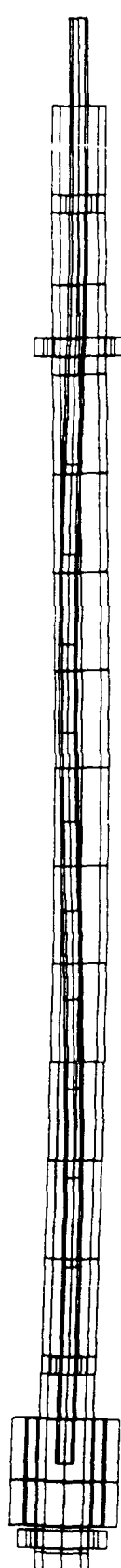
MODE: EQUILIBRIUM
FREQUENCY: 0 HZ



MODE: FIRST AND SECOND (DEGENERATE)
FREQUENCY: 24.5 HZ



MODE: THIRD AND FOURTH (DEGENERATE)
FREQUENCY: 88.8 HZ



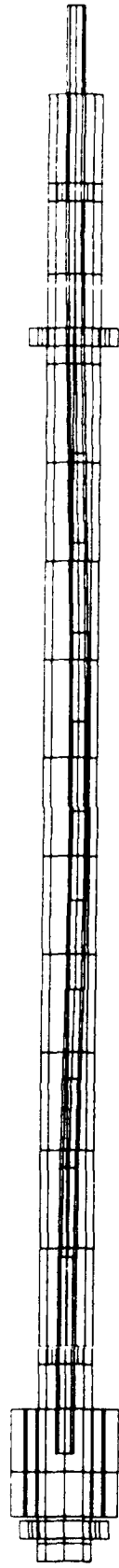
MODE: FIFTH AND SIXTH (DEGENERATE)
FREQUENCY: 213.1 HZ

BOUNDARY CONDITIONS: FREE / FIXED
SCALE: 1:1

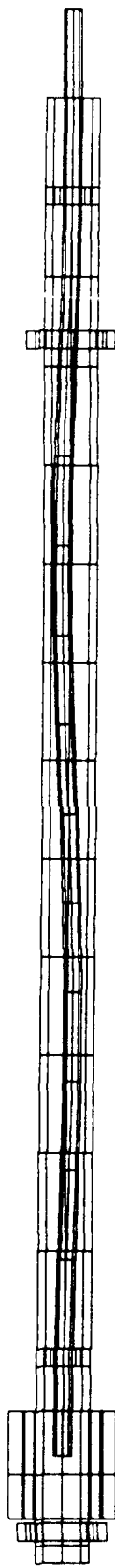
Figure 5(a)



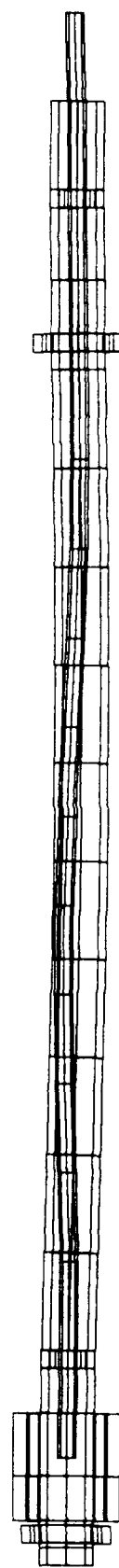
MODE: EQUILIBRIUM
FREQUENCY: 0 HZ



MODE: FIRST AND SECOND (DEGENERATE)
FREQUENCY: 86.7 HZ



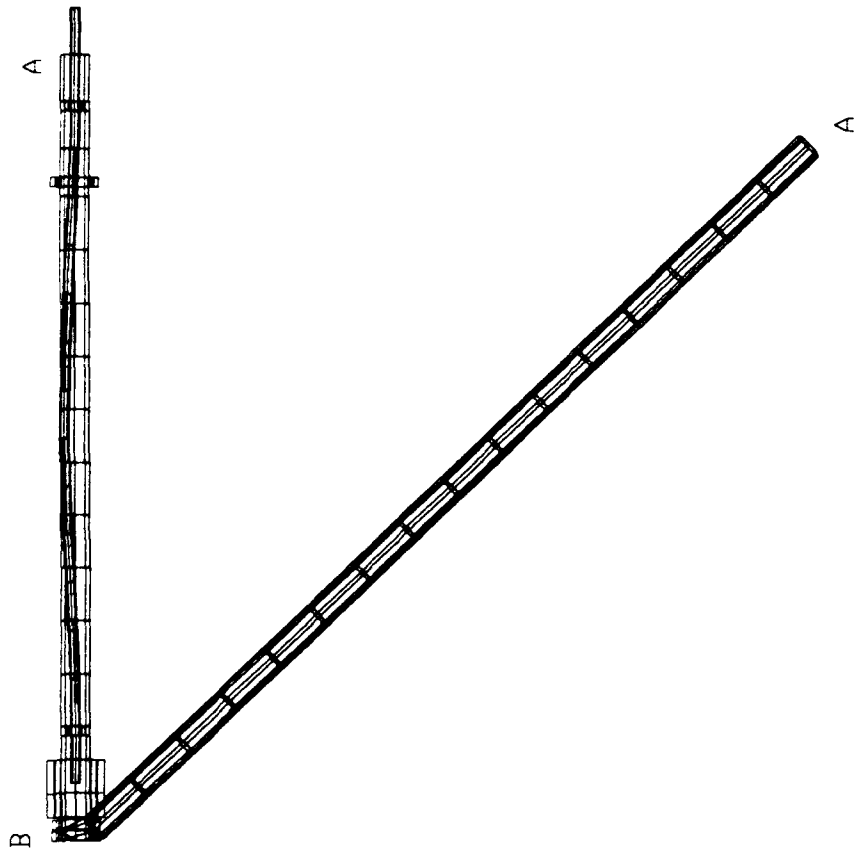
MODE: THIRD AND FOURTH (DEGENERATE)
FREQUENCY: 234.4 HZ



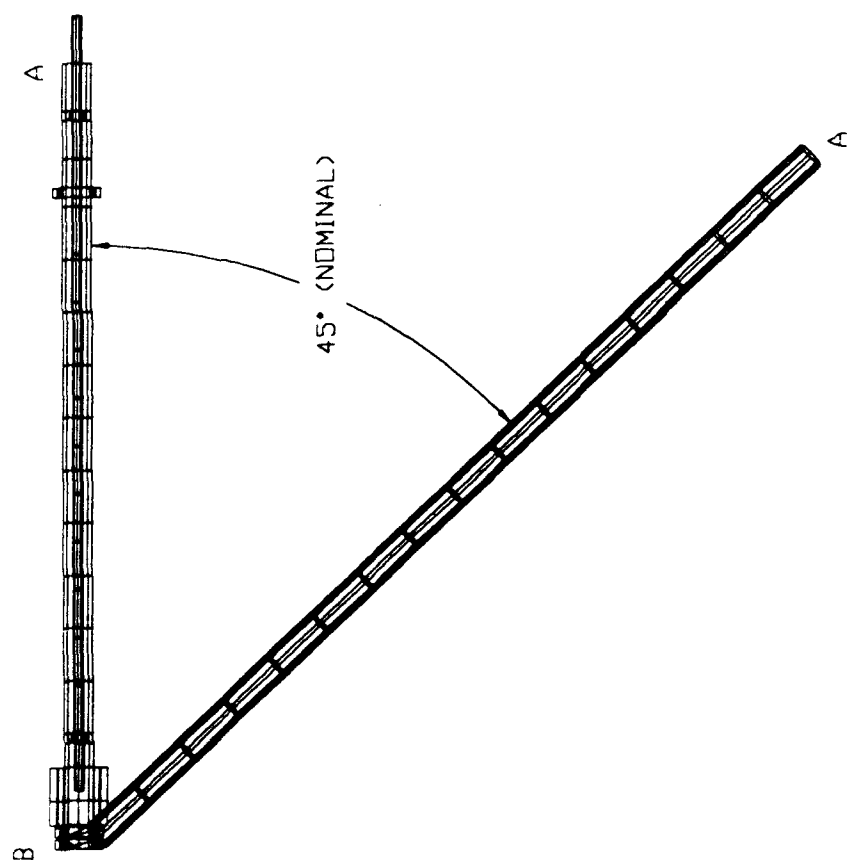
MODE: FIFTH AND SIXTH (DEGENERATE)
FREQUENCY: 244.0 HZ

BOUNDARY CONDITIONS: FIXED/FIXED
SCALE: 1.5

Figure 5(b)



MODE: SECOND
 FREQUENCY: 86.2 HZ



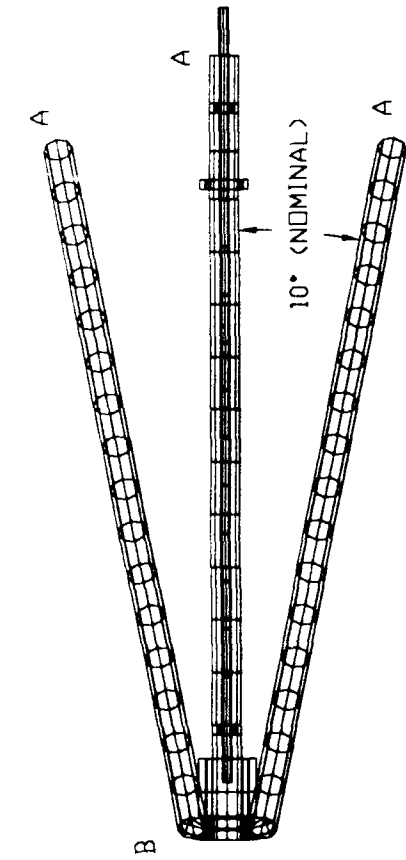
MODE: EQUILIBRIUM
 FREQUENCY: 0 HZ

45° (NOMINAL)

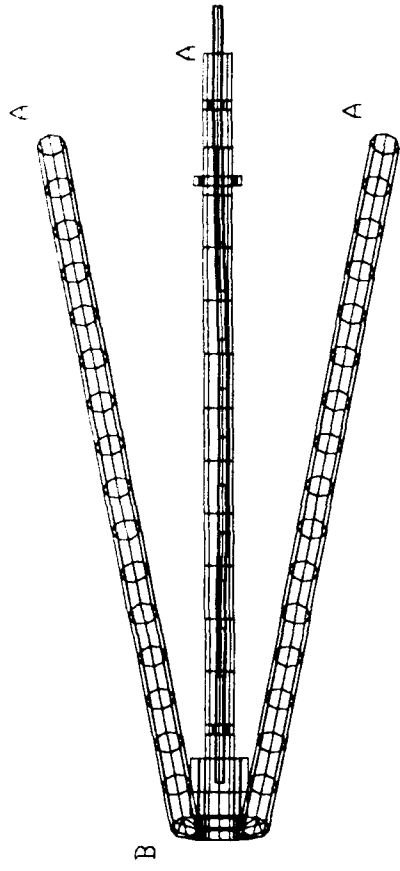
BOUNDARY CONDITIONS:
 A - FIXED
 B - FREE

SCALE: 1/10

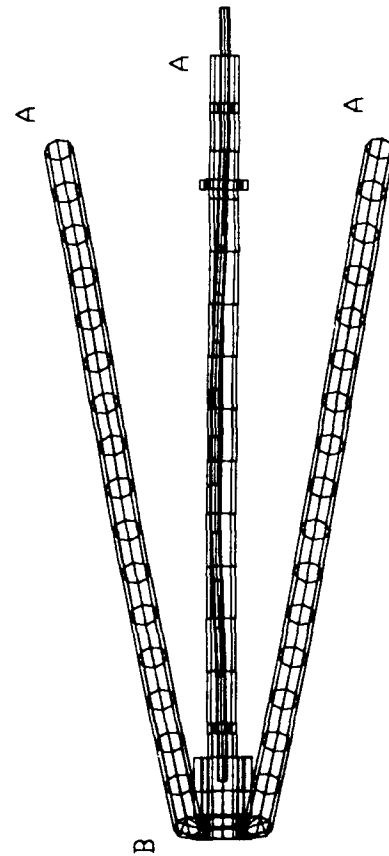
Figure 6(a)



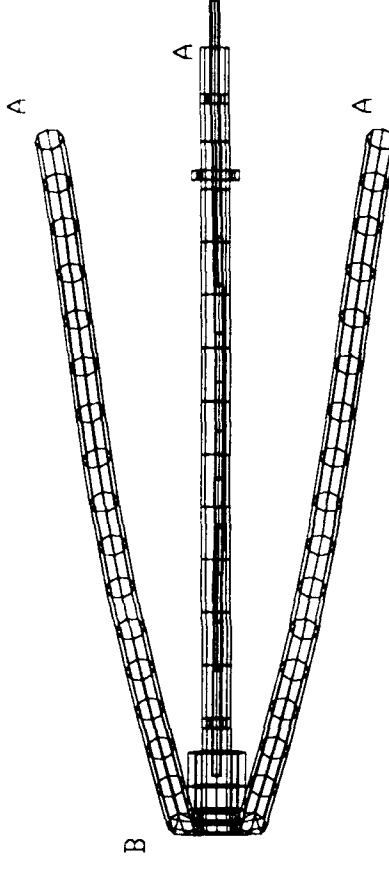
MODE: EQUILIBRIUM
 FREQUENCY: 0 HZ



MODE: THIRD
 FREQUENCY: 87.9 HZ



MODE: FIRST
 FREQUENCY: 61.1 HZ



MODE: FOURTH
 FREQUENCY: 97.1 HZ

BOUNDARY CONDITIONS:
 A - FIXED
 B - FREE

SCALE: 1:10

Figure 6(b)



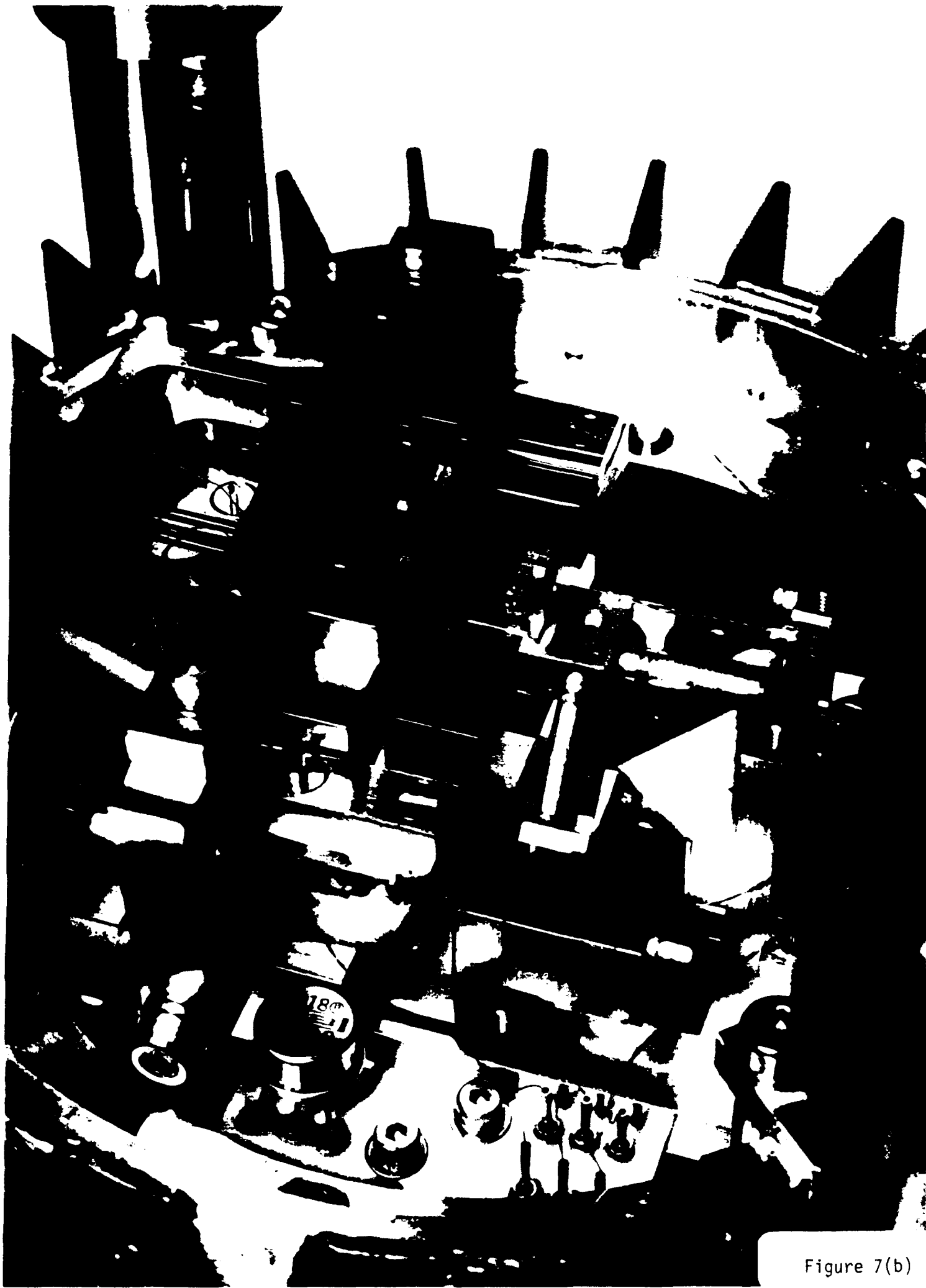
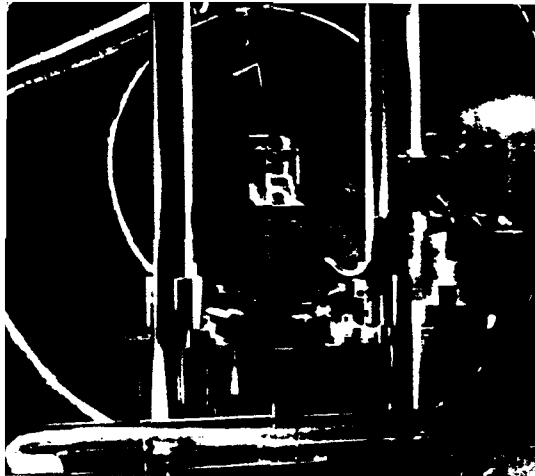


Figure 7(b)



EXTEND POSITION OF ENTRY
AREA WOBBLE STICK (WS 182)

SCALE: 1"=3"

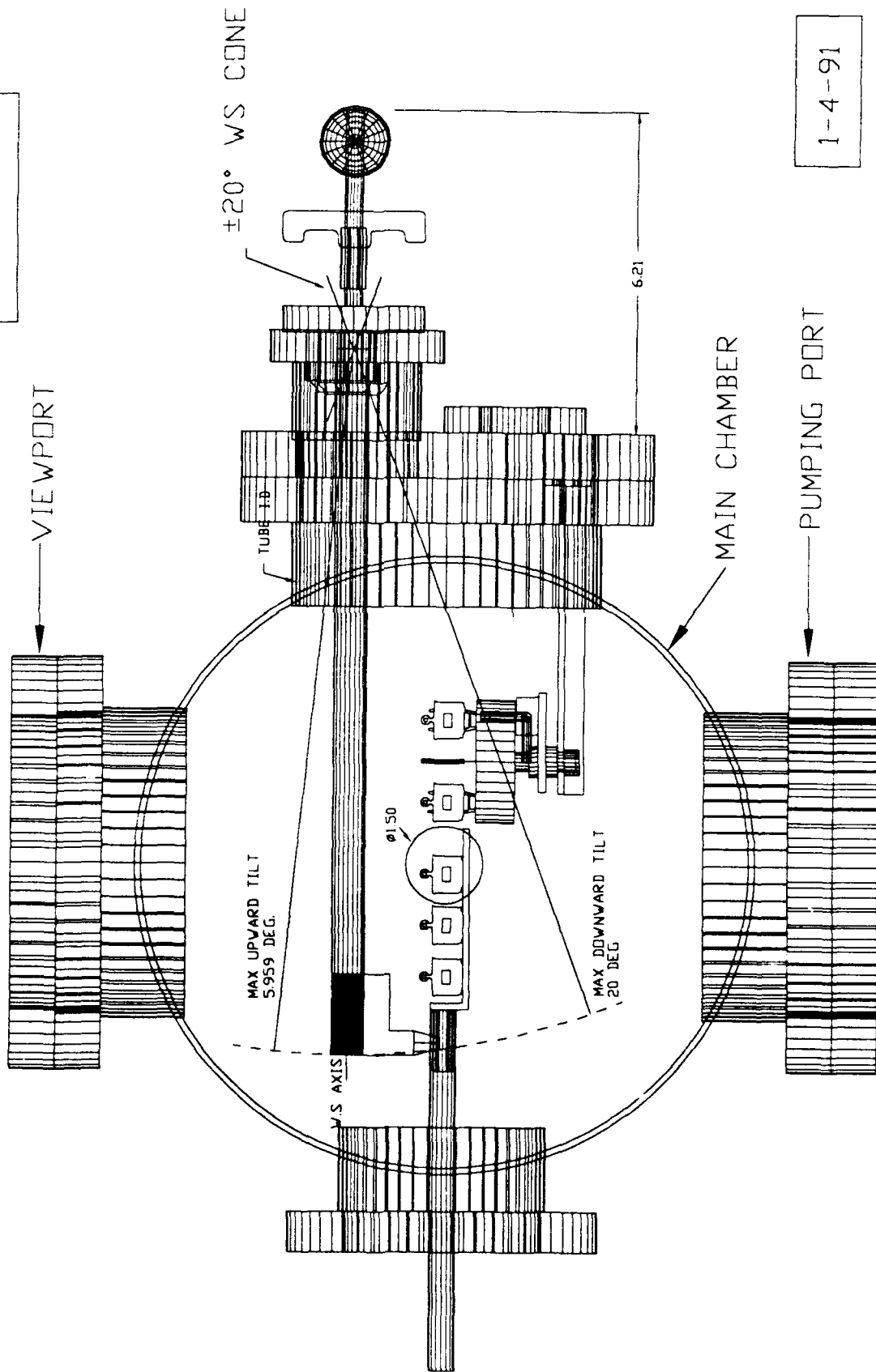
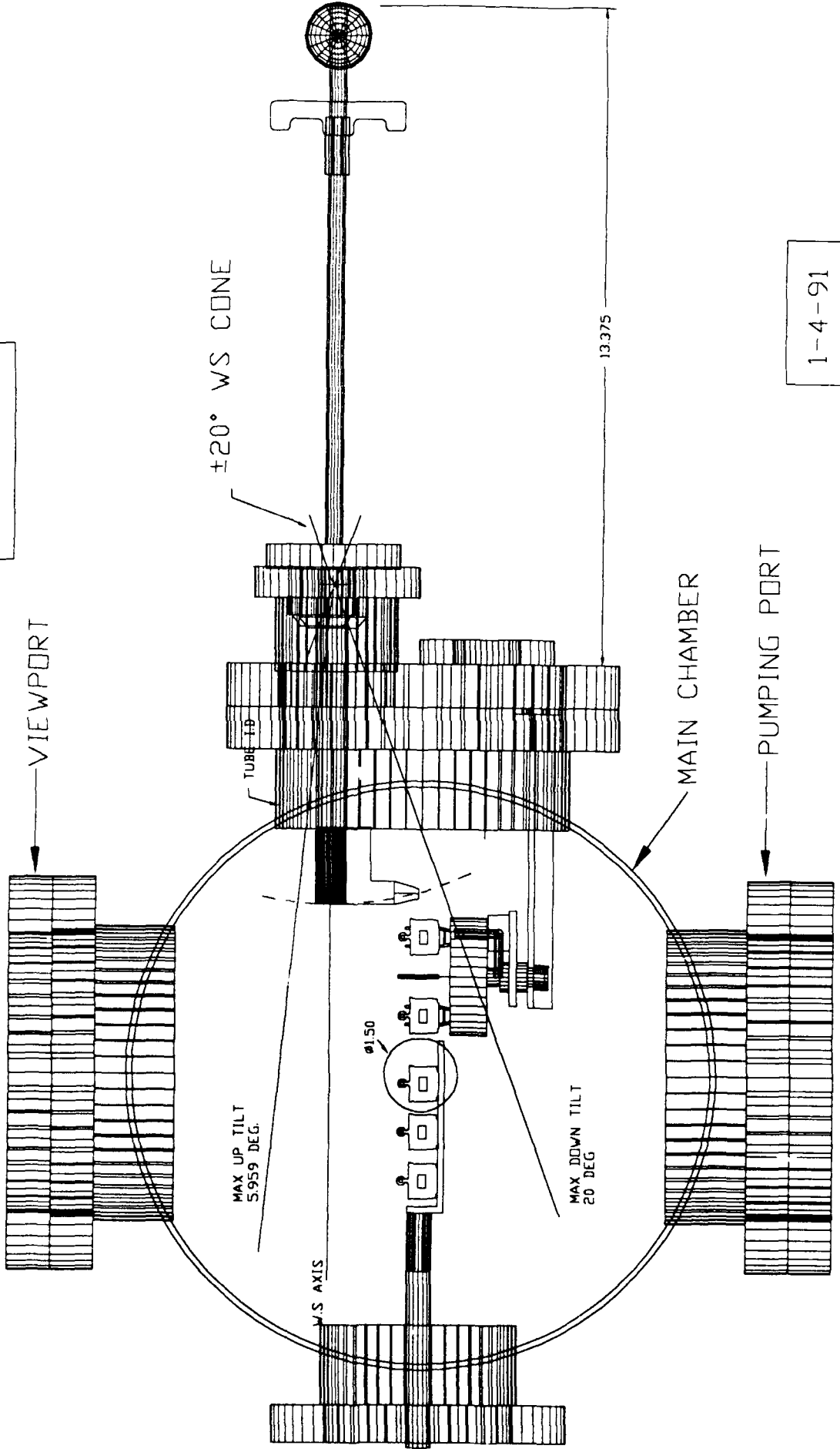


Figure 9(a)

RETRACTED POSITION OF ENTRY
AREA WOBBLE STICK (WS 182)

SCALE: 1"=3"



1-4-91

Figure 9(b)

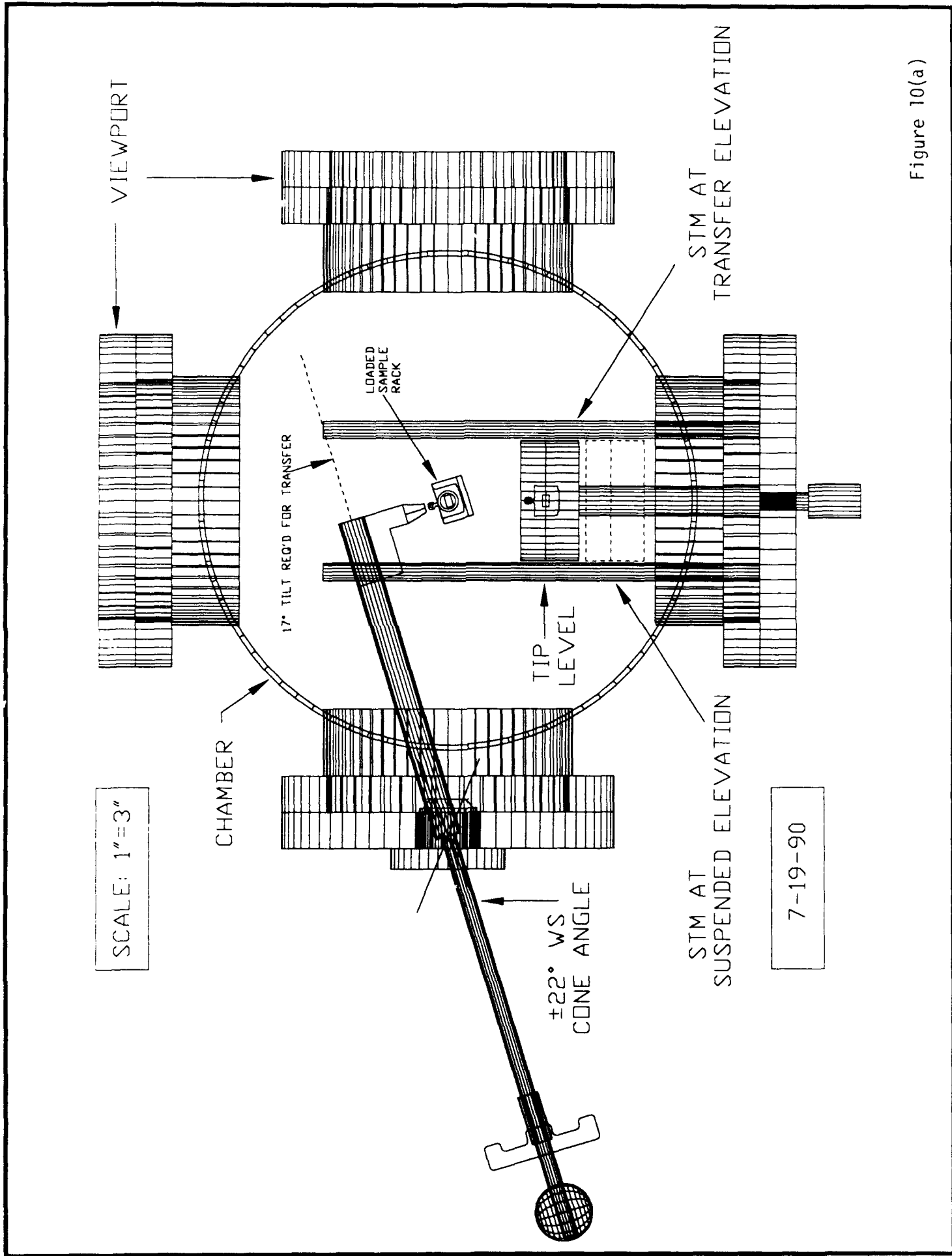


Figure 10(a)

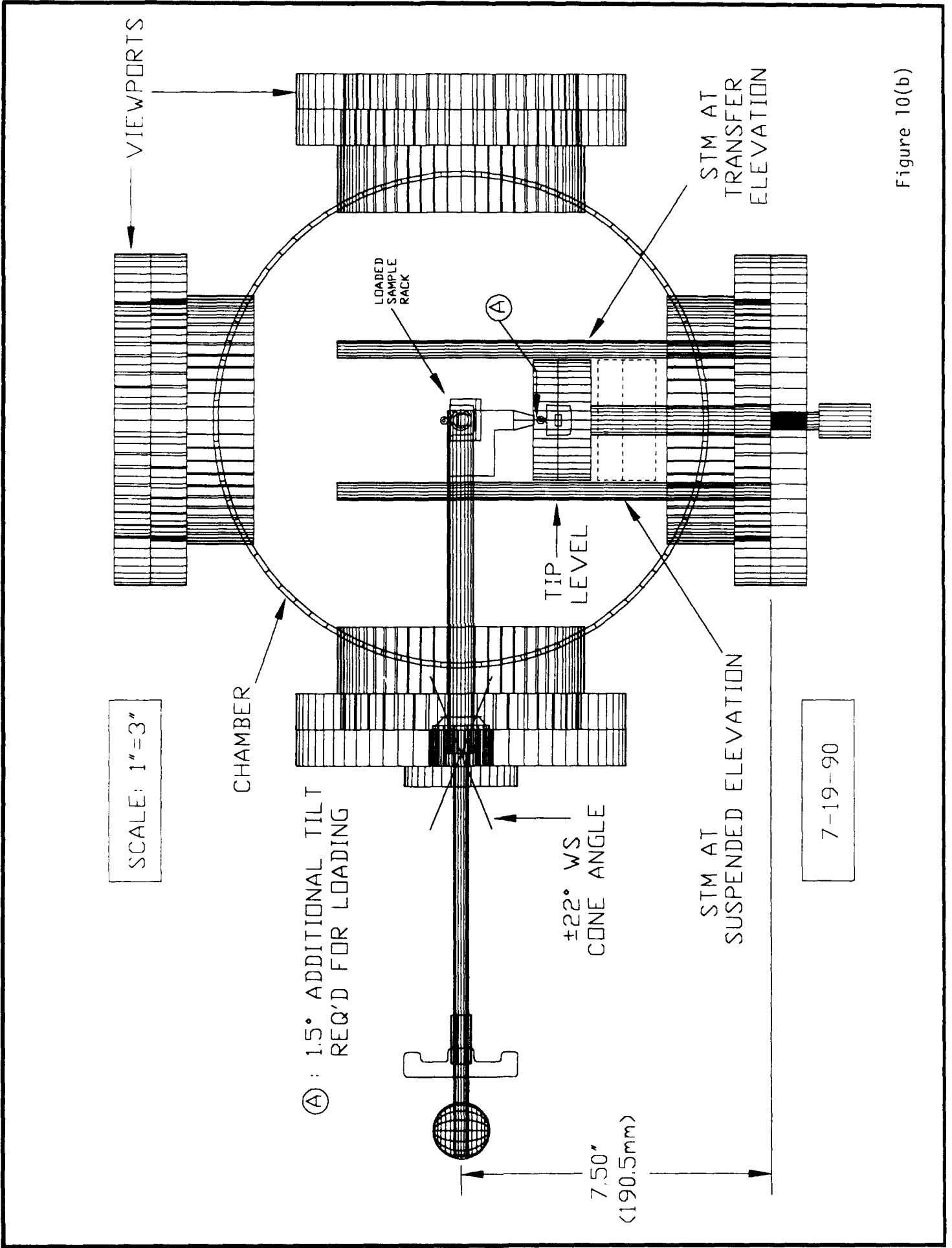


Figure 10(b)

Section III

AUGER SPECTROSCOPY

Figure Captions

Figure 1: Auger spectrum from copper test sample. The sample was sequentially cleaned using trichloroethane, acetone, and then ethanol, in an ultrasonic cleaner. The spectrum was taken with a Perkin Elmer 15-155 Cylindrical Mirror Analyzer.

<u>Peak</u>	<u>Energy</u>	<u>Element</u>
1	61	Cu
2	182	Cl
3	273	C
4	512	O
5	776	Cu
6	840	Cu
7	849	Cu
8	921	Cu

Figure 2: Auger spectrum from copper test sample. This part of the sample was etched in FeCl_3 to remove oxygen. Compare the ratio of peaks 4 and 8 to the same ratio in figure 1. Also note the ratio of peaks 3 and 8 in each figure. The magnitude of peak 2 in Figure 2 is due to the residue from the FeCl_3 .

<u>Peak</u>	<u>Energy</u>	<u>Element</u>
1	61	Cu
2	181	Cl
3	272	C
4	511	O
5	773	Cu
6	837	Cu
7	845	Cu
8	917	Cu

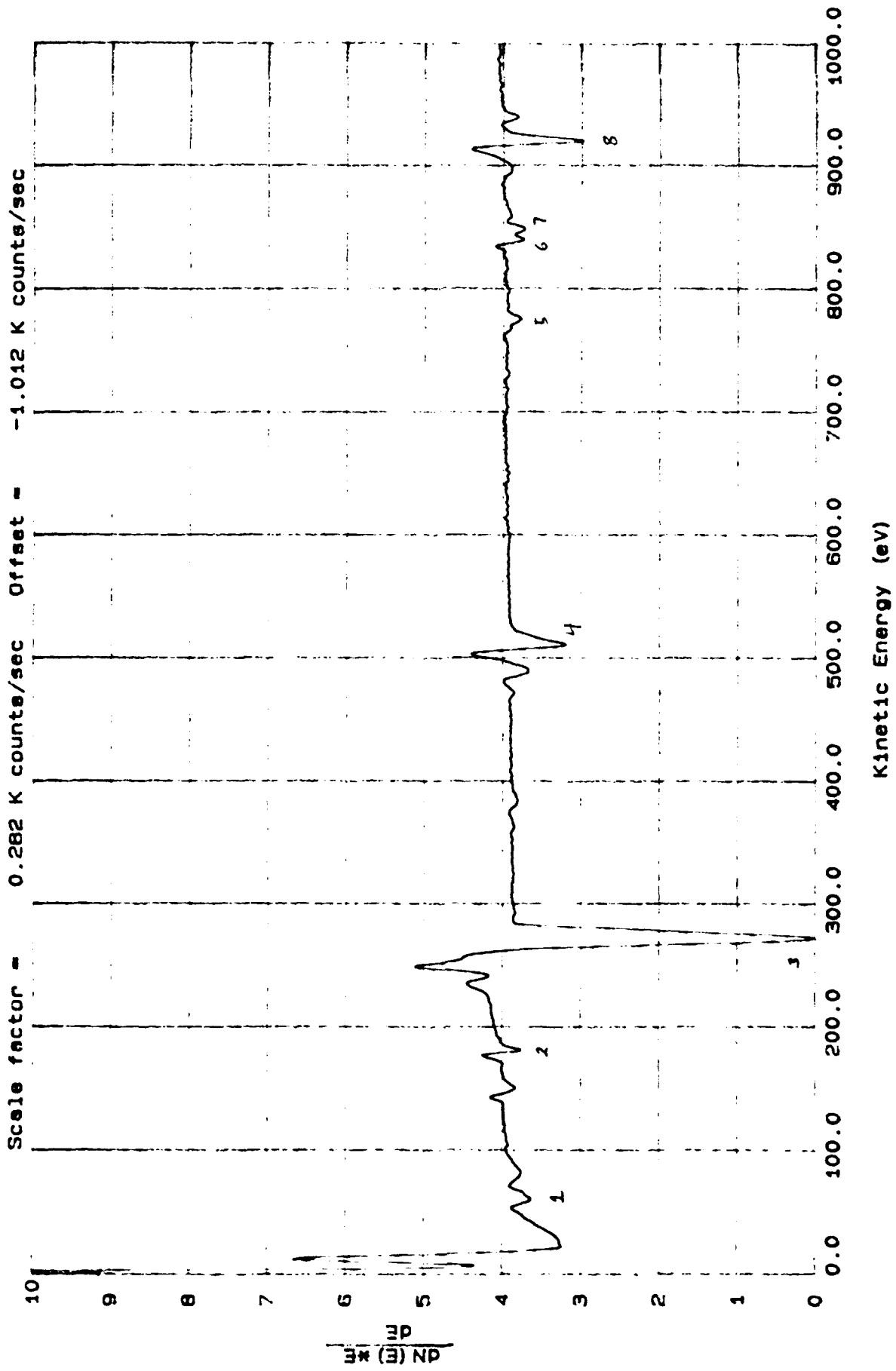


Figure 1

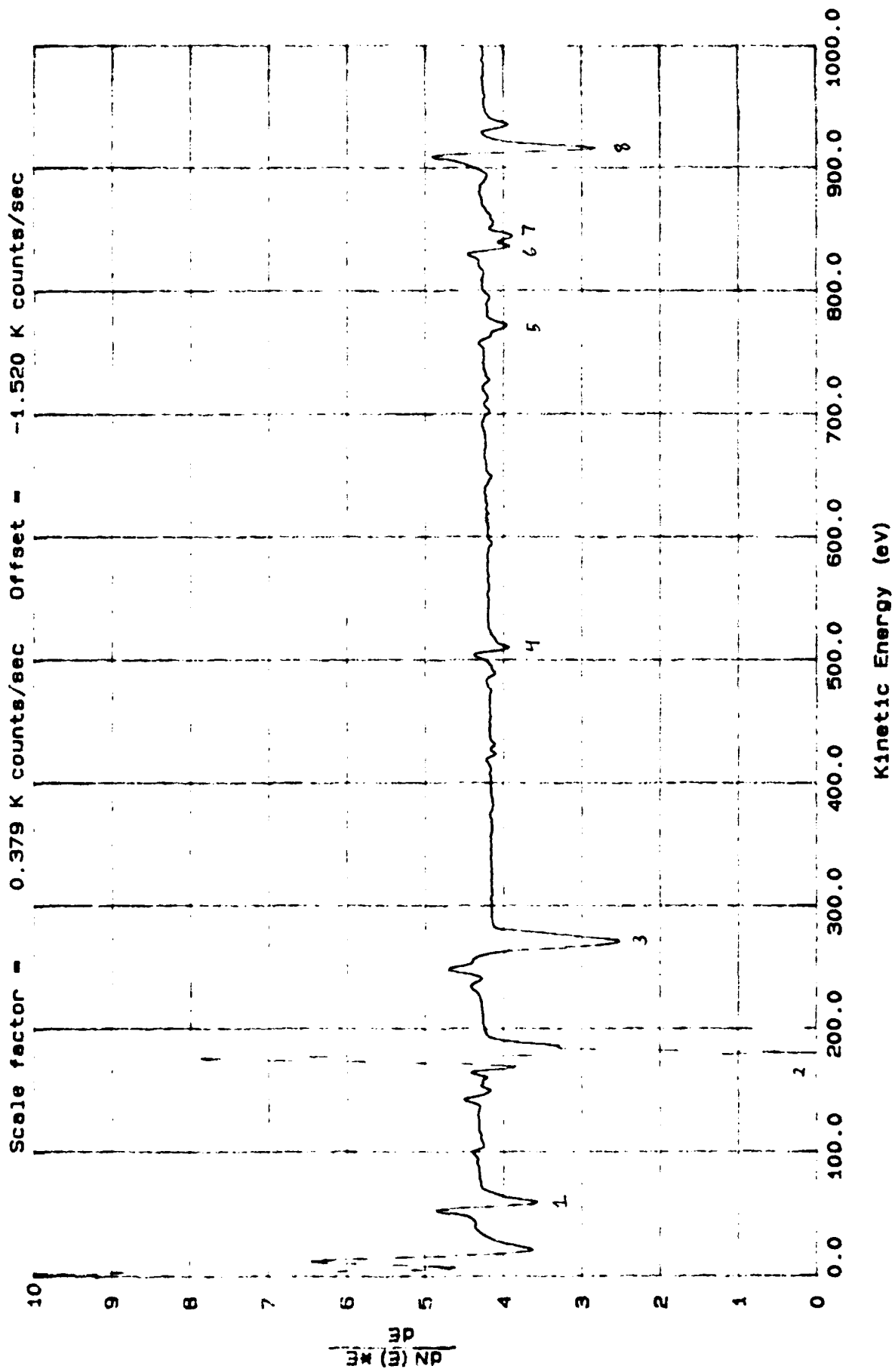


Figure 2

Section IV

TUNNELING MICROSCOPY

Figure Captions

Figure 1(a): UHV test data of a Si(111) 7x7 surface obtained with the instrument presently at Texas A&M. The sample was biased at 2.0V with a feedback current of 0.06nA. An atomic step is visible at the top of the image. This data was acquired at the Omicron factory.

Figure 1(b): A grey scale rendition of the same silicon image.

Figure 2(a): Topographic image of highly oriented pyrolytic graphite (HOPG) showing atomic resolution over a long (100 Angstrom) scan. The image was obtained in air with a platinum tip cut from wire. The sample bias was 50mV with a feedback current of 1.0nA.

Figure 2(b): Current image taken concurrently with the topographic image of Figure 2(a). The total time to take the data was 114 sec; the feedback time constant was set such that the atomic corrugation modulated the current.

Figure 3(a): Large area scan (2000 Angstroms by 2000 Angstroms) of the HOPG surface showing mono-atomic steps. The measured step height is about 3.4 Angstroms, in good agreement with the accepted value of 3.35 Angstroms.

Figure 3(b): A grey scale rendition of the same HOPG image.

Figure 4: Grey scale image of a tip crash site on HOPG. This distinctive feature could be imaged for hours and provided an opportunity to practice maneuvering the STM image frame.

Figure 5(a): A typical grey scale image of the surface of bulk gold. The large, rounded features such as these are commonly observed. This image was taken with a sample bias of 100mV and a feedback current of 1.0nA.

Figure 5(b): Another grey scale image of bulk gold. The data was obtained in air with a sample bias voltage of 2.5V and a feedback current of 0.05nA, yielding a nominal tunneling resistance of 50 gigaohms. Large, rounded features are resolved, but finer details are obscured presumably due to larger tip-sample separation than in 5(a).

Figure 6(a-c): Typical current-voltage (I-V) characteristics (left side of each figure) for junctions formed between a platinum STM tip and various samples: (a) graphite, (b) bulk gold, and (c) oxidized tungsten. Note that (a) and (b) have qualitatively different behavior near zero bias. The characteristics for graphite are less linear than the characteristics for gold. This is consistent with the greater difference in the work function values between graphite and platinum compared to gold and platinum. The oxidized tungsten characteristics behave similarly to those of a semiconductor. The right side of the figures shows the junction conductance, calculated by numerically differentiating the measured I-V characteristics. The effect of noise in this coarse data is readily apparent.

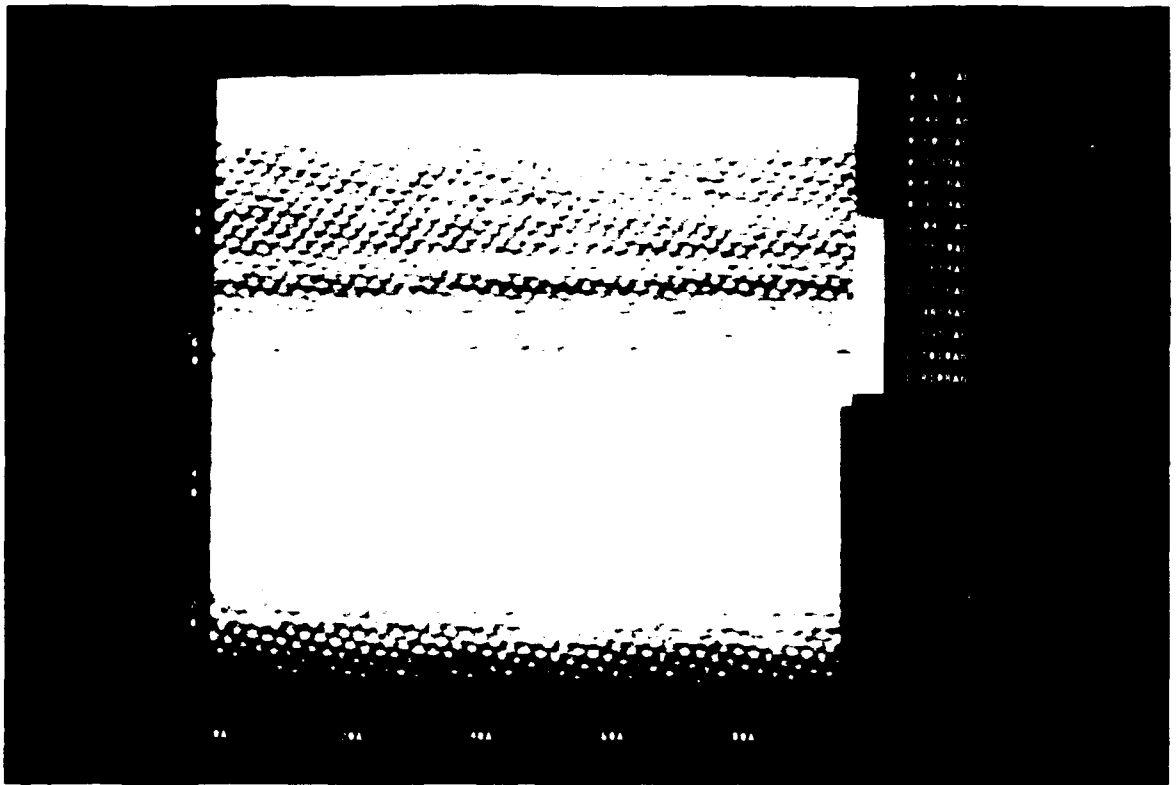


Figure 2(a)

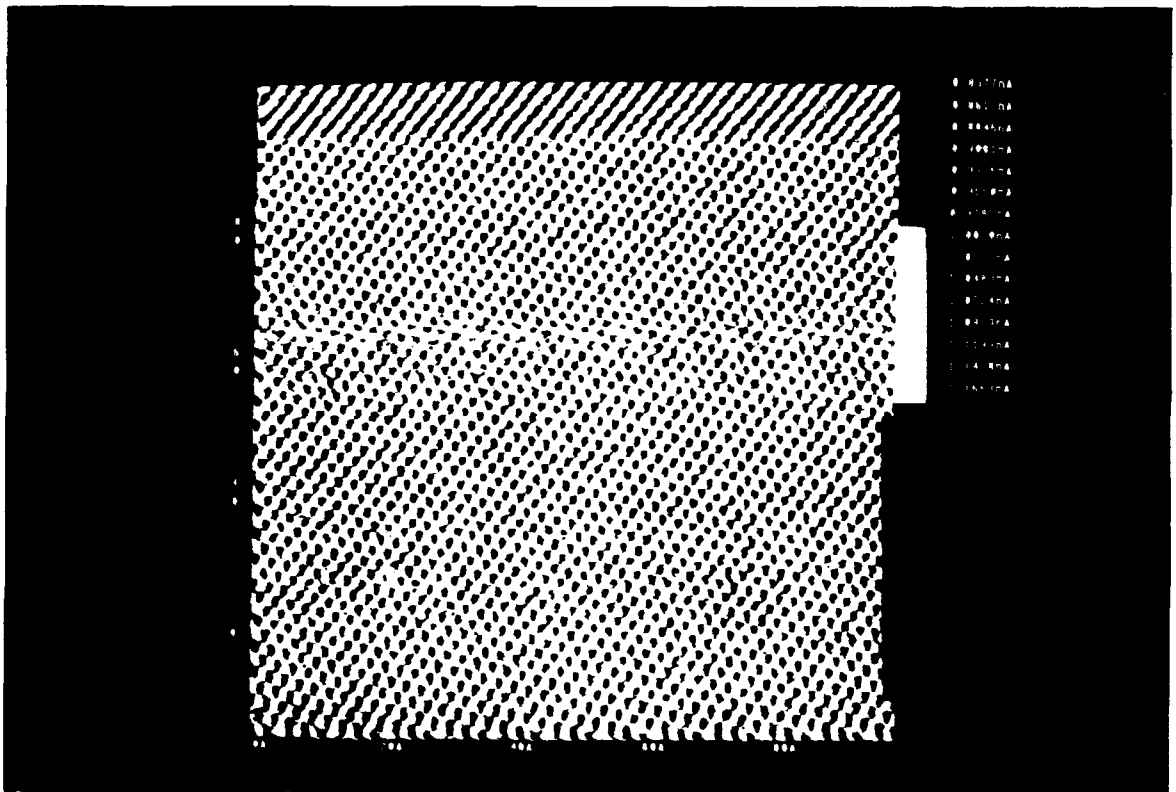


Figure 2(b)

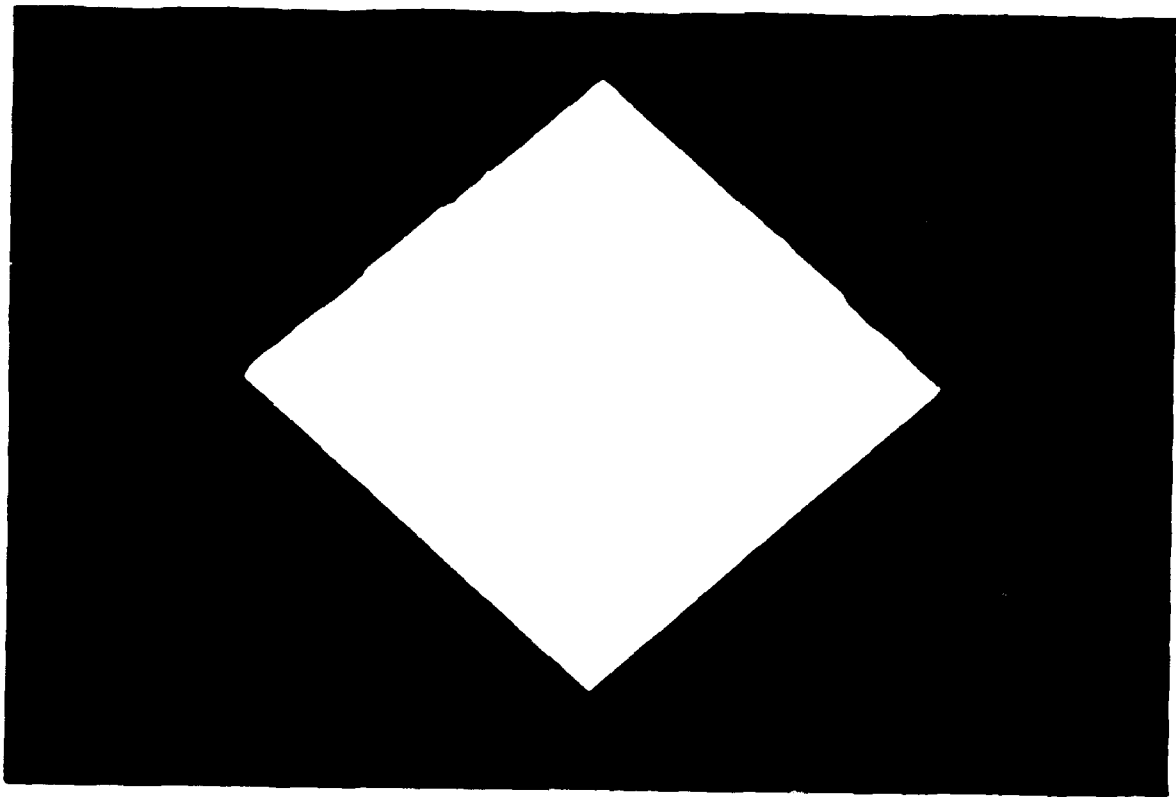


Figure 3(a)

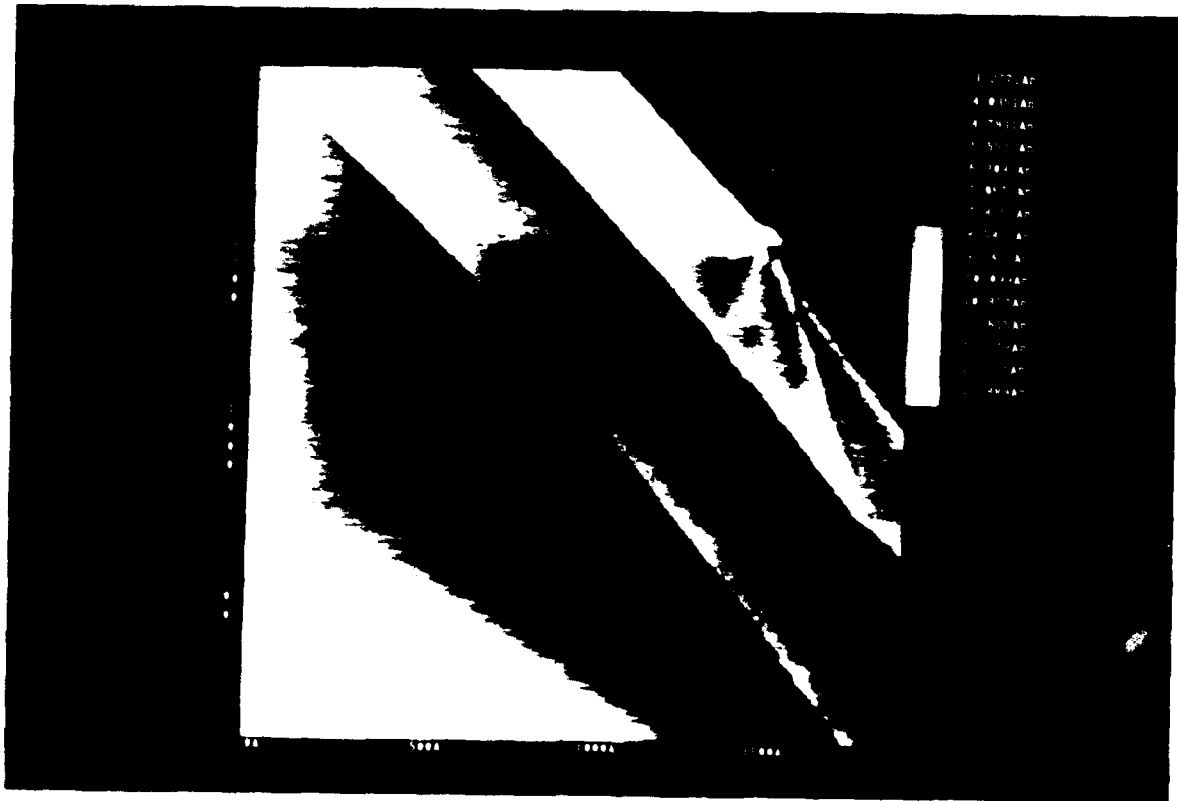


Figure 3(b)

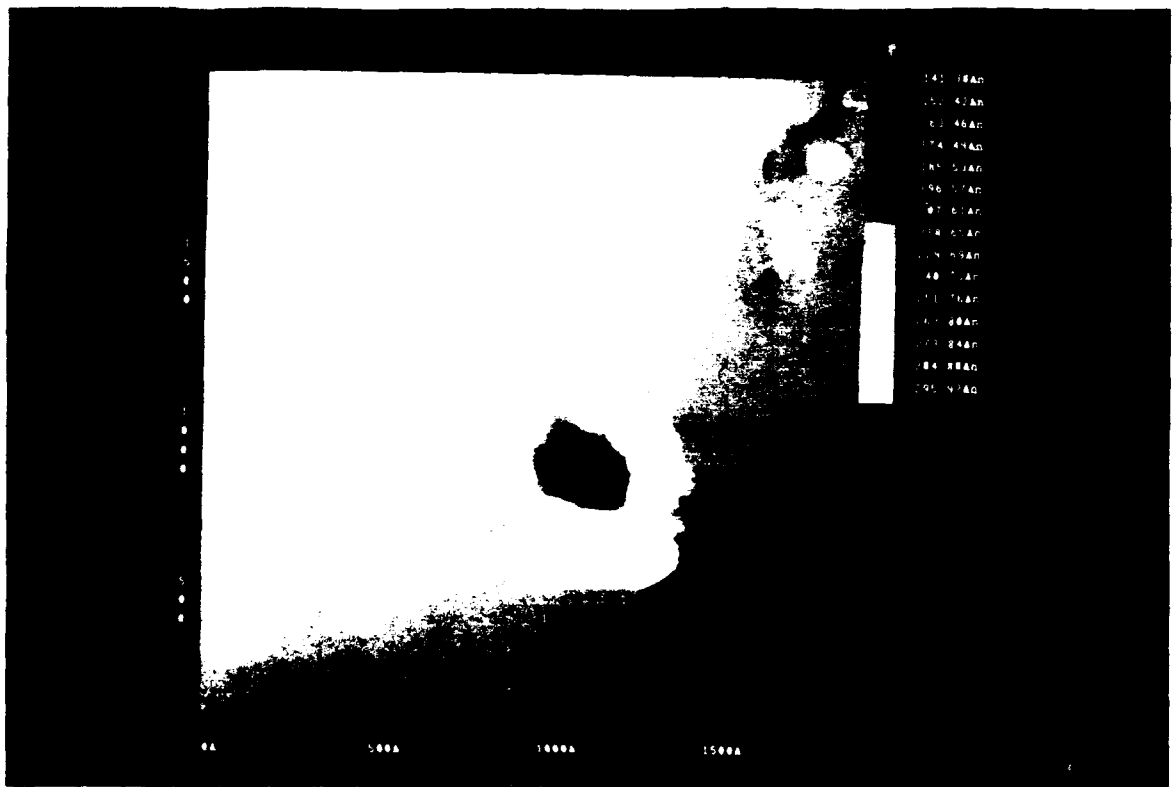


Figure 4

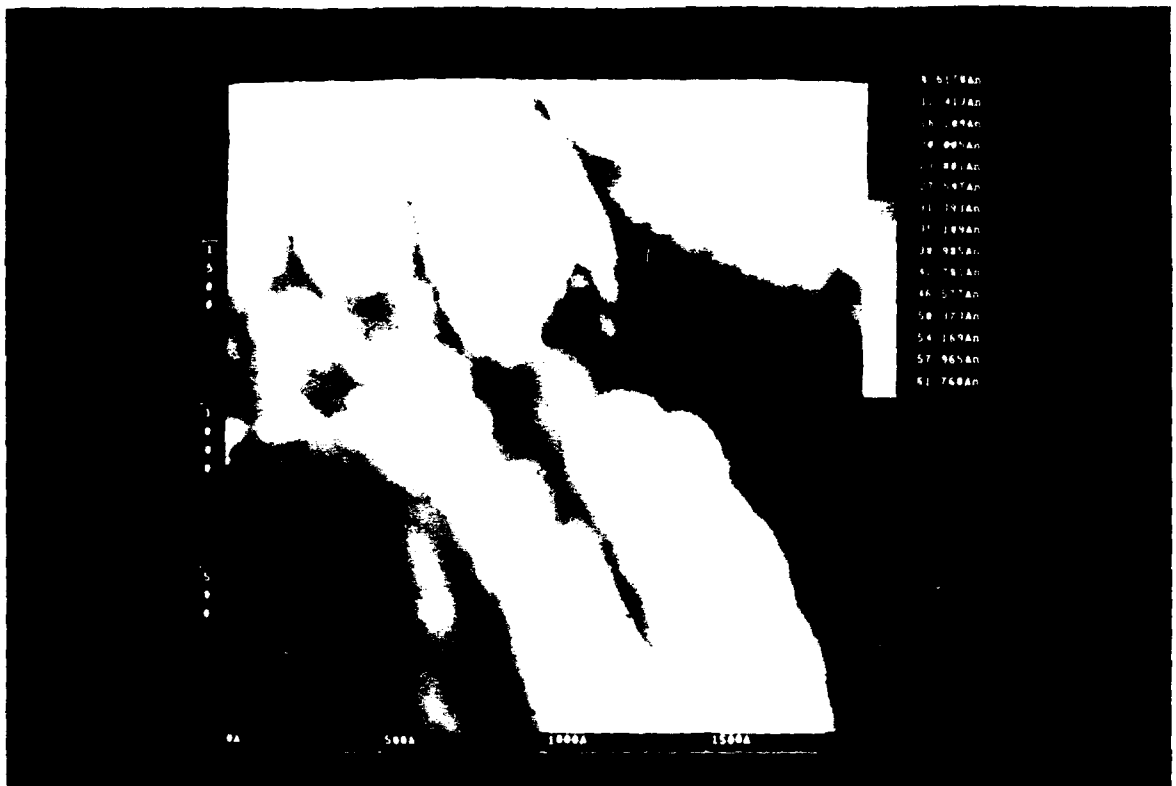


Figure 5(a)



Figure 5(b)

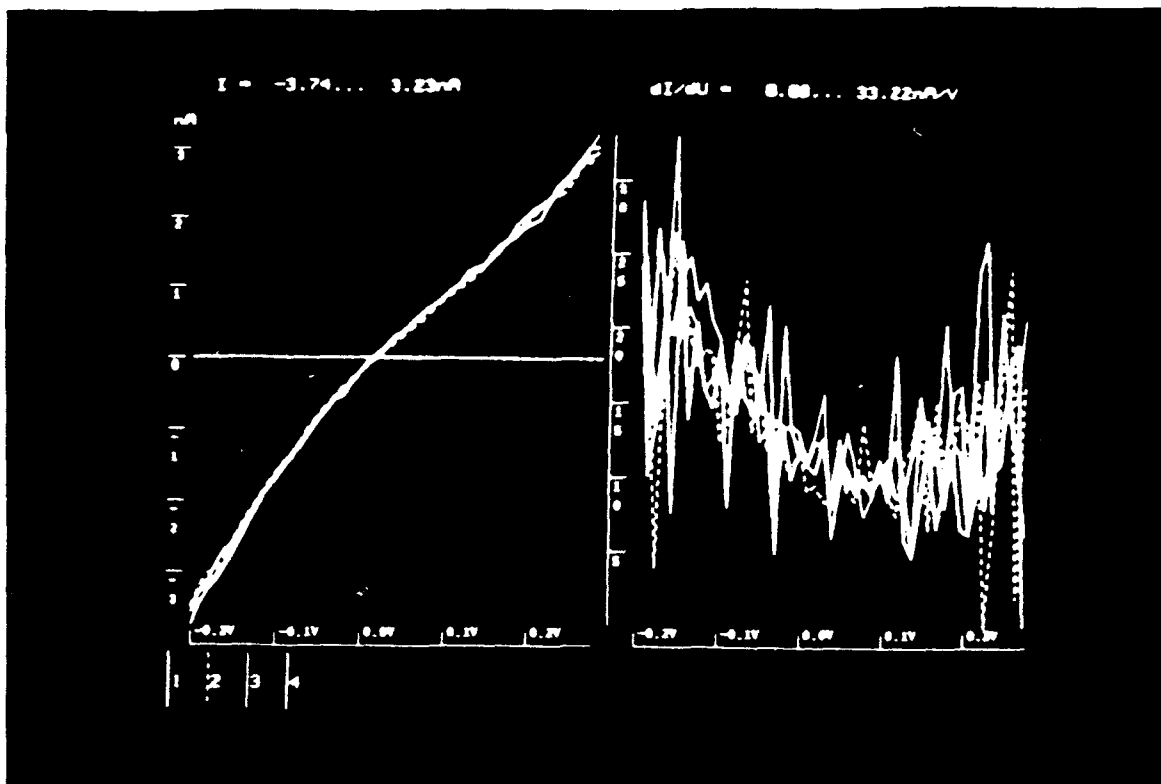


Figure 6(a)

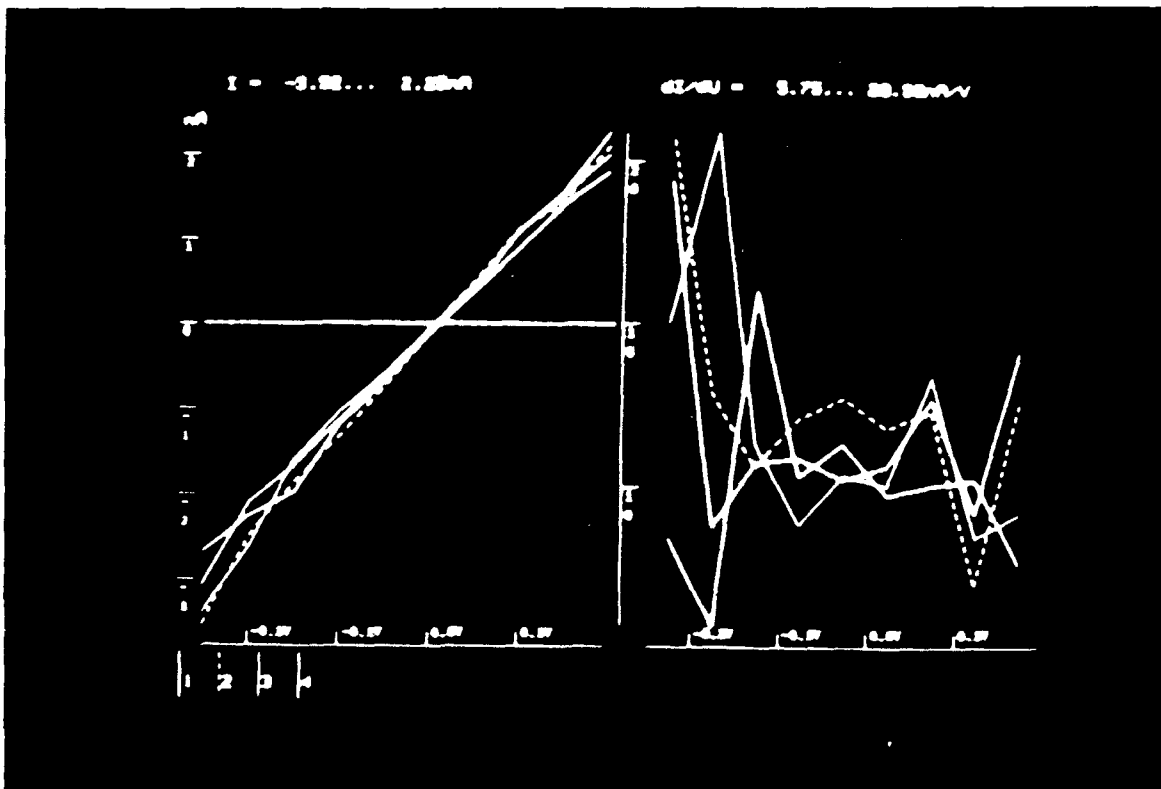


Figure 6(b)

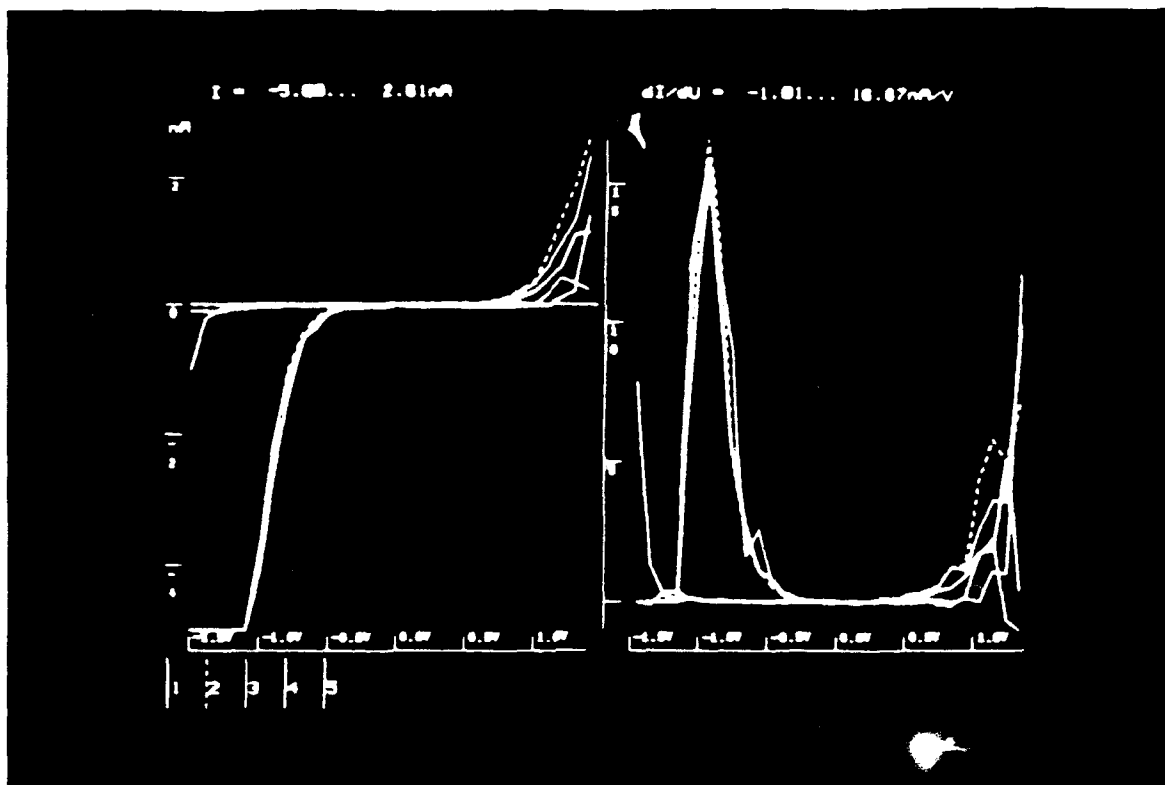


Figure 6(c)